

NUMERICAL HEAT TRANSFER – PART B: FUNDAMENTALS

<https://www.tandfonline.com/toc/unhb20/current>

Accepted April 28th, 2024.

Numerical study of hybrid binary Al₂O₃-Cu-H₂O nanofluid coating boundary layer flow from an exponentially stretching/shrinking perforated substrate with Cattaneo-Christov heat flux, heat source, suction and multiple slip effects.

K. Venkatadri¹, P. Sree Harshitha², O. Anwar Beg^{3*} and S. Kuharat^{3**}

¹ *Department of Mathematics, Indian Institute of Information Technology Sri City, Chittoor-517464, A.P., India.*

² *Department of Electronics and Communication Engineering, Indian Institute of Information Technology Sri City, Chittoor-517464, A.P., India.*

^{3*} *Professor and **Lecturer in Aeronautical Engineering, Multi-Physical Engineering Sciences Group, Mechanical Engineering Department, School of Science, Engineering and Environment (SEE), University of Salford, Manchester, UK.*

[^] *Corresponding author. Email: venkatadri.venki@gmail.com*

Co-author emails: O.A.Beg@salford.ac.uk; S.Kuharat2@salford.ac.uk

ABSTRACT:

Modern coating systems are increasingly deploying nanomaterials which offer improved thermal performance. The optimization of these systems can benefit from more elegant fluid dynamic models of the coating process. Inspired by these advancements, the present investigation introduces a novel mathematical model to analyze the boundary layer transport in Al₂O₃-Cu-H₂O hybrid binary nanofluid coating deposition on an exponentially stretching porous substrate (sheet). Lateral mass flux (suction) at the wall is also considered as is heat source (generation) for hot spot manufacturing effects. To add further sophistication to the thermal conduction model, a non-Fourier approach is adopted which accurately incorporates thermal relaxation effects i. e. the Cattaneo-Christov heat flux (CCHF) model. The Tiwari-Das volume fraction nanoscale formulation is implemented for different combinations of Alumina (Al₂O₃) and Copper (Cu) metallic nanoparticles in an aqueous base fluid (H₂O). Hydrodynamic wall and thermal slip are also included as they feature in coating processes. The fundamental equations governing mass, momentum, and energy conservation, along with the corresponding conditions at the wall (substrate) and free stream, are made dimensionless through suitable scaling similarity transformations. The resulting nonlinear coupled ordinary differential boundary value problem is subsequently addressed using the efficient MATLAB bvp4c routine. Special cases of the non-Fourier model are validated against published results, and the general model is further confirmed through validation using an Adams-Moulton 2-step predictor-corrector algorithm (AMPC).

Furthermore, dual solutions of the generalized model are extracted and visualized. A comprehensive study of the effects of key thermophysical key parameters on momentum and thermal characteristics (velocity, temperature, skin friction and local Nusselt number) is conducted and solutions are visualized graphically. The computations show that higher temperatures are present with an intensification in the thermal relaxation parameter (Cattaneo-Christov hyperbolic model parameter) which predicts therefore larger temperatures than the classical Parabolic heat conduction model using Fourier analysis. Effectively thermal relaxation is responsible for finite heat wave propagation and produces more accurate estimations of heat transfer than the Fourier model. An increase in stretching parameter enhances the skin friction coefficient and elevates the local Nusselt number. As the thermal relaxation parameter increases, the temperature magnitudes corresponding to the first and second solutions are both enhanced as are thermal boundary layer thicknesses. An increase in wall suction induces an escalation in the first solution for velocity whereas it reduces the second solution velocity. Stronger wall suction suppresses temperatures. With increasing thermal slip, the boundary layer is cooled i. e. temperature plummets and thermal boundary layer thickness is decreased. Strong deceleration is induced with greater hydrodynamic (velocity) slip. Both first and second solutions for skin friction are elevated with shrinking whereas they are depressed with stretching. With greater velocity slip both the first and second solutions for skin friction are depleted with greater velocity slip for the shrinking case, whereas they are generally enhanced for the very strong stretching case. The computations offer some new insights into multi-physical thermal fluid dynamics of nanofluid-based coating systems.

KEYWORDS: *Non-Fourier conduction model, hybrid Al_2O_3 -Cu- H_2O binary nanofluid coating, dual solutions, stretching/shrinking sheet, coating flows, wall suction, hydrodynamic and thermal slip, MATLAB bvp4c.*

NOMENCLATURE:

ROMAN

(A_1, B_1)	: velocity (hydrodynamic) and thermal slip parameters
(A, B)	: velocity and thermal slip dimensionless parameters
C_f	: local skin friction coefficient
C_p	: specific heat capacity
q	: heat generation parameter
T	: fluid temperature
T_w	: wall temperature
(u, v)	: velocity components in x and y directions

u_w	: velocity of the substrate surface
v_w	: wall mass transfer (transpiration) velocity
v_0	: mass suction (<0) & the mass injection (>0)
Nu_x	: local Nusselt number
Pr	: Prandtl number
Re_x	: local Reynolds number
S	: suction parameter (<0) & mass injection (>0)

GREEK

α	: thermal relaxation parameter.
β	: heat generation parameter
λ	: the wall stretching constant (>0)/shrinking constant (<0) & static sheet (=0)
ρ	: nanofluid density
ν	: kinematic viscosity
(ϕ_{s1}, ϕ_{s2})	: alumina and copper nanoparticle volume fraction parameters
μ	: dynamic viscosity
ψ	: dimensional stream function
η	: non-dimensional transverse coordinate

RKFM	: Runge – Kutta – Fehlberg Method
CCHF	: Cattaneo-Christov heat flux
AMPC	: Adams-Moulton 2-step predictor corrector
TRT	: Thermal relaxation time

1. INTRODUCTION

Heat transfer proficiency has become a key issue in the 21st century owing to significant environmental and sustainability concerns. Cooling is a critical issue in optimizing thermal systems. For example, normal refrigerants have limitations and conventional working fluids also fall short in many regards with respect to thermal efficiency. Nanofluids have emerged as a very promising solution to circumventing these issues. These complex colloidal suspensions are engineered at the nanoscale and synthesized with nanoparticles (size 100 nm) suspended in conventional base fluids e. g. water, glycol and oil. Metals, oxides, graphite, nitrides, nanotubes and carbides are some examples of nanoparticles which have been successfully implemented in nanofluids in the 21st century. Many studies have been conducted to establish the physical mechanisms which contribute to enhanced thermal efficiency to nanofluids. These include nanoparticles, heat conduction, Brownian movement, thermophoresis, micro-convection, slip, etc., Since its discovery in the 1980s, nanotechnology has been at the forefront of modern technology and has enabled engineers to effectively manipulate individual atoms at the nanoscale. When a solid substance possessing higher thermal conductivity is mixed with a base fluid of lower thermal conductivity, the resulting nanofluid produces enhanced thermal characteristics. Thermal conductivity and heat capacity are both improved. This progress has been documented in many literature reviews, including Can *et al.* [1] where many applications of nanofluids are elaborated. The new generation of nanomaterials developed have achieved enhanced strength, stiffness, toughness, durability, functionality, corrosion resistance, anti-bacterial etc. Many efficient, affordable, and eco-friendly products have been produced based on nanomaterial breakthroughs. Nanofluids have impacted on numerous areas including battery heat management as addressed by Hamzat *et al.* [2]. Further applications of nanofluids include solar collectors [3], bio-inspired electromagnetic solar pumps [4], engine coolants [5], endoscopic peristaltic micro-pumps [6], lubricants for machine components [7], magnetic fuel cells [8], jet engine fuels [9], thermal ducts in nuclear reactors [10] and rocket propellant combustion [11]. Another significant area in which nanofluids have been utilized is coatings technology. Nanoparticles can be embedded in traditional coating fluids to produce substantial improvements in wear and toughness and to achieve more consistent protection of engineering devices against environmental degradation. They can provide superior corrosion, anti-bacterial and insulating performance. Many different nanoparticles, both carbon-based and metallic, have been explored in a range of coating systems. These include chromium, Nickel and carbon nanoparticles for high velocity fuel spraying deposition [12], iron

oxide and zinc-manganese nanoparticles for ferromagnetic swirl coating [13], diamond and alumina nanoparticles in spin coating [14], Cerium oxide nano-composite coatings [15], titanium and Niobium nano-coatings for marine vessel surface protection [16] and cobalt alloy laser nano-coatings [17]. Manufacturing of nano-coatings involves a variety of fluid dynamics technologies including plasma deposition and enrobing. Another procedure, film stretching or shrinking [18, 19] of nano-coatings on a continuous substrate has stimulated considerable interest among scientists in recent years as it provides an excellent framework for boundary layer flow modelling. Stretching flows have been studied by Nasir *et al.* [20] for nano-lubricant films, Qu *et al.* [21] for stretchable zin-air battery coatings and Almansoori *et al.* [22] for multi-functional nano-films. Nanofluid mathematical models of coatings have also received considerable attention. Two methods have been popular in these investigations- the *Buongiorno two-phase nanoscale model* (which includes energy and conservation of nanoparticle species equations) and the *Tiwari-Das volume fraction approach* (which only includes energy balance but allows for different nanoparticle materials to be simulated). Other formulations include the Maxwell-Garnetts model. The Tiwari-Das and Maxwell-Garnetts models are essentially single-phase approaches in which all appropriate nanofluid properties (density, viscosity and thermal conductivity etc) are formulated with an appropriate volume fraction. Stretching or shrinking may be linear, quadratic, exponential or combinations of these types. This involves using a wall velocity with the appropriate expression. Venkateswarlu and Narayana [23] investigated numerically the performance of water-based nanoliquid stretching/shrinking sheet flows with the RKFM and shooting algorithms. Bég *et al.* [24] reported the magnetic nano-film stretching flow of a solar nano-coating with induction effects. Siddiqui *et al.* [25] investigated homogeneous and heterogeneous chemical reaction effects on copper and alumina aqueous nanocoating flow from a stretching cylindrical body with entropy generation. Gharvandha *et al.* [26] studied computationally the phase change and radiative flux impact on boundary layer nanofluid coating of a tilted cylinder under the impact of chemical reaction and curvature effects. Uddin *et al.* [27] analyzed the hydrodynamic and thermal slip effects on Buongiorno nanofluid coating boundary layer flow from a linearly extending/contracting sheet. Further studies include Latiff *et al.* [28] (on time-dependent micropolar nanofluid bioconvection flow past a stretching/ shrinking sheet) and Thumma *et al.* [29] (on hydromagnetic magnetized nanofluid flow over a tilted stretching or

contracting substrate with viscous heating). All these studies showed that stretching or shrinking significantly modifies the momentum and thermal characteristics of nanofluid coatings.

The above studies have all been restricted to the *Fourier heat conduction model*. This model however utilizes a parabolic energy equation. This has remained the popular standard approach in thermal conduction for almost 200 years [30]. However, the Fourier model assumes that the material experiences an initial disturbance and erroneously predicts infinite thermal wave speed propagation in heat conduction. To address the inconsistency issue, Cattaneo [31] proposed heat conduction model using Fourier analysis. This modification led to a more realistic model of finite-speed heat conduction, resulting in a hyperbolic model. The model was further refined by Christov [31], leading to the development of the CCHF model, a modern version of the non-Fourier model. The "thermal inertia" in this model involves a change to Fourier's law brought about via the inclusion of a TRT factor. Owing to the limitations of the classical Fourier law effectively the law of cause and effect is invalidated. In dealing with a fluid theory of the Cattaneo type, Christov [31] emphasized the importance of the objective derivative and successfully substituted the derivative for the Oldroyd upper-convexion time derivative, thereby preserving the material-invariant formulation. Straughan [32] further confirmed the robustness of the CCHF model for a wide range of initial and boundary value problems in thermal conduction. Additional stability aspects of the CCHF model were scrutinized by Ciarletta and Straughan [33]. Tibullo and Zampoli [34] established uniqueness results for the Cattaneo-Christov heat flux model in incompressible fluid dynamics. Numerical solutions for incompressible Newtonian thermal convection flow with the Cattaneo-Christov were presented initially by Straughan [34] and later by Haddad [35] using the tau-D₂ Chebyshev technique. In recent years, many engineering scientists and mathematicians have organized the Cattaneo-Christov in a range of transport problems including nano-coating flows, thermal injection molding polymer processing, squeezing lubrication, rotational film deposition etc. In the context of solid body heat transfer, the Fourier model is a widely used macroscopic description that accounts for infinitesimal heat disturbances. However, under certain conditions, such as time interruptions in thermal transfer in real materials, the non-Fourier (CCHF) model has been found to be more accurate in capturing these effects. In many computational studies, this model has been shown to determine temperature fields more accurately, which tends to be over-predicted by the Fourier model. A diverse range of numerical schemes has been adopted to solve the complex nonlinear boundary value problems arising in materials processing

applications. Hayat *et al.* [36] used the semi-numerical Lioa homotopy analysis method (HAM) to compute higher order solutions for thermal stagnation flow of a viscoelastic Jeffreys coating over a nonlinear variable-thickness stretching sheet. They incorporated dual thermal/solutal stratification and chemical reaction influences, observing that higher non-Fourier TRT parameter values lead to the suppression of both temperature and thermal boundary layer thickness. In a subsequent study, Hayat *et al.* [37] analyzed the impact of CCHF on the stagnation flow of Maxwell non-Newtonian fluid over a nonlinear stretching surface with variable thickness. This analysis considered dual homogeneous and heterogeneous reactions, employing a homotopy method once again. They confirmed that with thermal relaxation present, temperatures are reduced compared to when it is absent (Fourier model) attributing this to the time delay in thermal conduction between material particles. Nasir *et al.* [37] presented homotopy perturbation solutions for mixed convection in magnetized coating flow of Reiner–Rivlin second-grade electro-conductive nanofluid polymer past a stretching sheet in a porous medium with the CCHF and non-Fickian mass diffusion models. They used the Buongiorno two-component mixed nanoscale model to simulate Brownian motion and thermophoretic body force effects. They noted that higher values of non-Fourier thermal and non-Fickian solutal relaxation parameters exert the converse influence on temperature and nanoparticle concentration fields. Many other interesting studies have been communicated using the Cattaneo–Christov non-Fourier heat flux model including Gul *et al.* [40] (magnetized nanofluid slip flow with autocatalytic chemical reaction), Zhang *et al.* [41] (phase change in swirling gold-silver/engine oil nanofluid flow), Waqas *et al.* [42] (entropy generation in nozzle nanofluid dynamics), Shaik Jakeer *et al.* [43] (hydromagnetic enclosure nanofluid flow), Muhammad *et al.* [44] (squeezing nanofluid film flow with a finite difference technique) and Kumaran *et al.* [45] (enrobing coating dynamics with bio-magneto-nanofluids using Keller’s box method).

Building on the success of unitary i.e. single nanoparticle material-type nanofluids, engineers have further explored mixtures of diverse nanoparticles. This has led to the emergence of a new subset of nanofluids which are termed hybrid nanofluids. The material nanoparticles are suspended in a base fluid by suspending two (or more) distinct nanoparticles. Hybrid nanofluids have been shown to achieve even more superior enhancement in thermal efficiency relative to unitary nanofluids or regular fluids. *Binary nanofluids* refer to two nanoparticles being used simultaneously. *Ternary nanofluids* are produced when three different nanoparticles are deployed. Both one-step and two-

step processes remain popular for synthesizing hybrid nanofluids. Since the different nanoparticles in hybrid nanofluids possess different diffusion rates, thermal conductivities and other properties, they can be manipulated to achieve optimized heat exchange performance in diverse manufacturing systems including surface deposition and coatings, heat capacitors, vehicle power generation, heat pumps, aircraft wing skin designs and microelectronics. Many combinations of nanoparticles have been explored in recent studies of nanofluid stretching/shrinking sheet coating dynamics. Prakash *et al.* [46] adopted a finite element approach to study the performance of graphene oxide, molybdenum and copper hybrid nanoparticles in electro-magnetic rotating coating flow of a stretching substrate with wall suction effects. Devi and Devi [47] computed the magnetohydrodynamic copper-alumina aqueous nanofluid flow from a porous extending sheet with strong wall suction effects. Shamshuddin *et al.* [48] investigated the relative performance of Molybdenum and Molybdenum disulphide (MoS_2) nanoparticles on rotating MHD generator flow in EO oil Brinkman nanofluids. They utilized Laplace Transform technique and complex variables and observed that MoS_2 nanoparticles achieve better thermal and pumping efficiency than molybdenum nanoparticles (unitary nanofluid) alone. Many other interesting studies have been conducted of hybrid nanoparticles in a range of applications including Tripathi *et al.* [49] (gold/silver-blood nanofluid), Prakash *et al.* [50] (viscoplastic nanofluids with gold, zinc and copper ternary hybrid nanoparticles in thermal electro-osmotic stirring), Al-Kouz *et al.* [51] (Fe_3O_4 /carbon nanotube (CNT) binary hybrid magnetic nanofluid solar collectors using COMSOL Galerkin finite element software), Ghandi *et al.* [52] (binary gold/alumina hybrid nanoparticles in arterial nano-pharmacodynamics), Bhatti *et al.* [53] (magnetic Magnesium oxide/Nickel binary hybrid nanoparticles in solar coating stagnation flow) and Mahabaleshwar *et al.* [54] (copper and alumina hybrid nanoparticles in nanofluid reactive boundary layer coating flow on a permeable stretching sheet). Further studies include Bhatti *et al.* [55] (hybrid (gold/magnesium) nanoparticles in electromagnetic gel propellant heat transfer), Thirumalaisamy *et al.* [56] (iron oxide/multi-walled carbon nanotube hybrid nanoparticles with different base fluids in magnetic fuel cells), Sumithra *et al.* [57] (solar magnetic direct absorber collectors with copper/alumina hybrid nanoparticles), Venkatadri *et al.* [58] (titanium oxide/copper hybrid nanoparticles in porous medium solar absorbers), Latha *et al.* [59] (graphene oxide, gold, cobalt oxide hybrid nanoparticles in EO base nanofluids), Reddy *et al.* [60] (hybrid $\text{Ti}_6\text{Al}_4\text{V-AA7075}/\text{H}_2\text{O}$ nanofluids in electromagnetic sensor near-wall flows) and Elsebae *et al.* [61] (magnesium oxide, titanium

dioxide and cobalt ferrite hybrid nanoparticles in stretching sheet coating flow with activation energy effects).

An inspection of the scientific literature on hybrid nanofluid coating has shown that thus far the *non-Fourier boundary layer coating slip flow of Al_2O_3 -Cu- H_2O hybrid binary nanofluid from an exponentially stretching porous substrate (sheet) with wall suction and heat generation effects* has not been considered. The novelty of the current computation is therefore the simultaneous consideration of *both thermal and velocity slip, exponential wall stretching, thermal relaxation effects i. e. the CCHF model, wall suction, heat source and hybrid nanoparticles (copper and alumina) with a Tiwari-Das volume fraction nanoscale formulation*. Additionally, a detailed dual solution analysis [62-65] is conducted. The basic equations governing mass, momentum, and energy conservation, along with the corresponding conditions at the wall (substrate) and in the free stream, are transformed into dimensionless forms using suitable scaling similarity transformations. The emerging nonlinear coupled ordinary differential boundary value problem is then solved with the efficient MATLAB bvp4c routine. Validation of special cases of the non-Fourier model with published results is included. Dual velocity i. e. first and second solutions of the generalized model are extracted and visualized. An in-depth exploration of essential parameters on momentum and thermal characteristics is conducted and solutions are visualized graphically. The simulations conducted have direct and immediate practical implications in nanofluid coating manufacturing processes and constitute an important generalization to existing studies.

2. PROBLEM FORMULATION

Steady-state incompressible hybrid nanofluid boundary layer coating flow from an exponentially stretching or shrinking non-isothermal porous substrate is considered. Mass flux at the wall is permitted and heat generation is present due to a hot spot. The non-Fourier CCHF effect model is deployed. The hybrid nanofluid is a dilute stable colloidal suspension and contains copper and alumina nanoparticles suspended in an aqueous base fluid. **Fig. 1** depicts the physical model for both stretching and shrinking case scenarios, in an (x, y) coordinate system where x is in the direction of stretching/shrinking and y is transverse to it. The surface velocity is $u_w(x) = ce^{\frac{x}{L}}$, wall

mass flux exponential velocity is $v_w(x) = v_0 e^{\frac{x}{2L}}$, non-isothermal wall temperature is $T_w = T_\infty + T_0 e^{\frac{x}{2L}}$ and heat generation $q = q_0 e^{\frac{x}{L}}$. Following Pandey *et al.* [66], and extending their Fourier model to the non-Fourier CCHF, the governing conservation equations for the flow can be shown to take the form:

$$\frac{\partial u}{\partial x} + \frac{\partial u}{\partial y} = 0 \quad (1)$$

$$u \frac{\partial u}{\partial x} + v \frac{\partial u}{\partial y} = \frac{\mu_{hmf}}{\rho_{hmf}} \frac{\partial^2 u}{\partial y^2} - \frac{\mu_{hmf}}{k_p \rho_{hmf}} u \quad (2)$$

$$u \frac{\partial T}{\partial x} + v \frac{\partial T}{\partial y} = \frac{\kappa_{hmf}}{(\rho C_p)_{hmf}} \frac{\partial^2 T}{\partial y^2} + \frac{q}{(\rho C_p)_{hmf}} (T - T_\infty) - \lambda_1 \left(\begin{aligned} &u \frac{\partial u}{\partial x} \frac{\partial T}{\partial x} + v \frac{\partial v}{\partial y} \frac{\partial T}{\partial y} + u \frac{\partial v}{\partial x} \frac{\partial T}{\partial y} + v \frac{\partial u}{\partial y} \frac{\partial T}{\partial x} \\ &+ 2uv \frac{\partial^2 T}{\partial x \partial y} + u^2 \frac{\partial^2 T}{\partial x^2} + v^2 \frac{\partial^2 T}{\partial y^2} \end{aligned} \right) \quad (3)$$

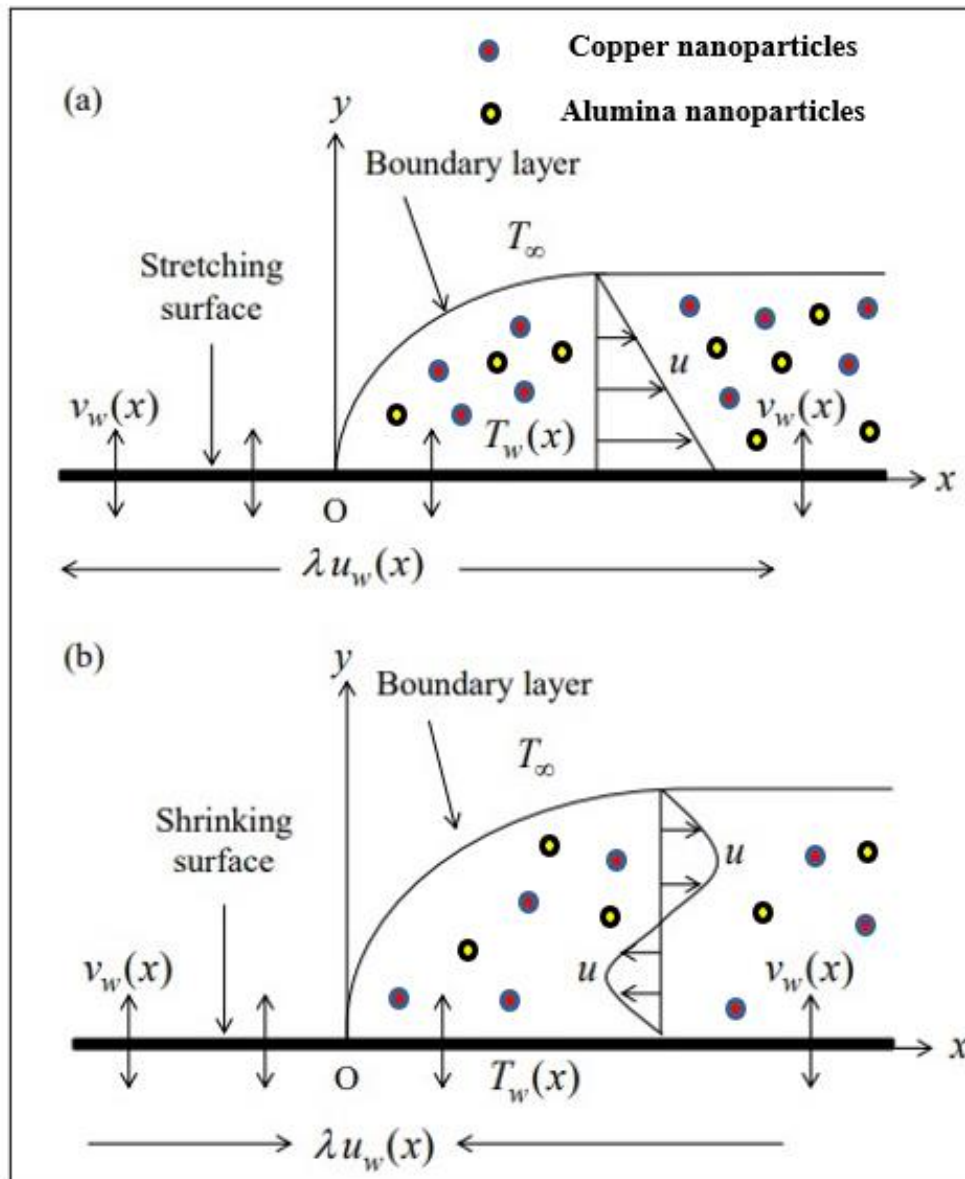


Figure 1: Physical model - (a) stretching (b) shrinking substrate.

The boundary conditions with hydrodynamic and thermal wall slip are imposed as:

$$u = \lambda u_w(x) + A_1 \frac{\mu_{hnf}}{\rho_{hnf}} \frac{\partial u}{\partial y}, v = v_w, T = T_w(x) + B_1 \frac{\partial T}{\partial y} \quad \text{at} \quad y = 0 \quad (4)$$

The free stream boundary conditions are:

$$u \rightarrow 0, T \rightarrow T_\infty \quad \text{as} \quad y \rightarrow \infty \quad (5)$$

To render the primitive partial differential boundary layer problem, dimensionless, the following scaling transformations are implemented following Pandey *et al.* [66] and Hayat *et al.* [67]:

$$\begin{aligned} \psi &= e^{\frac{x}{2L}} \sqrt{2\nu_f L c} f(\eta), \quad u = \frac{\partial \psi}{\partial y}, \quad v = -\frac{\partial \psi}{\partial x}, \quad \theta(\eta) = \frac{T - T_\infty}{T_w - T_\infty}, \quad \eta = ye^{\frac{x}{2L}} \sqrt{\frac{c}{2\nu_f L}}, \\ \text{Pr} &= \frac{(\mu C_p)_f}{k_f}, \quad \beta = \frac{2q_0 L}{c(\rho C_p)_f}, \quad A = A_1 \left(\frac{\mu_{hmf}}{\rho_{hmf}} \right) e^{\frac{x}{2L}} \sqrt{\frac{c}{2\nu_f L}}, \quad B = B_1 e^{\frac{x}{2L}} \sqrt{\frac{c}{2\nu_f L}}, \\ S &= -\frac{v_0}{\sqrt{\left(\frac{\nu_f c}{2L} \right)}}, \quad \alpha = \frac{\lambda_1}{\nu}. \end{aligned} \quad (6)$$

Introducing Eqn. (6) in Eqns. (1)-(5), we have:

$$\left(\frac{\mu_{hmf}}{\rho_{hmf}} \frac{\mu_f}{\rho_f} \right) f'''' + f f'' - 2f'^2 - Da \left(\frac{\mu_{hmf}}{\rho_{hmf}} \frac{\mu_f}{\rho_f} \right) f' = 0 \quad (7)$$

$$\frac{1}{\text{Pr}} \left(\frac{k_{hmf}}{k_f} \right) \theta'' + \frac{(\rho C_p)_{hmf}}{(\rho C_p)_f} (f \theta' - f' \theta) + \beta \theta - \alpha \left\{ \begin{array}{l} 0.75 f f' \theta' + 0.5 f'^2 \eta \theta' + \\ 0.5 f f'' \theta + f'^2 \theta + 0.25 f^2 \theta'' \end{array} \right\} = 0 \quad (8)$$

The modified conditions at the boundary become apparent as:

$$f(0) = S, \quad f'(0) = \lambda + Af''(0), \quad \theta(0) = 1 + B\theta'(0) \quad (9)$$

$$f'(\eta) \rightarrow 0, \quad \theta(\eta) \rightarrow 0 \quad \text{as} \quad \eta \rightarrow \infty \quad (10)$$

Regarding the local level skin-friction coefficient and Nusselt number, the provided expressions are as follows:

$$C_f = \frac{\mu_{hmf}}{\rho_f} \frac{1}{u^2 w} \left(\frac{\partial u}{\partial y} \right)_{y=0}, \quad Nu_x = \frac{k_{hmf}}{k_f} \frac{-2L}{(T_w - T_\infty)} \left(\frac{\partial T}{\partial y} \right)_{y=0} \quad (11)$$

The dimensionless skin friction coefficient and reduced local Nusselt number by virtue of Eqn. (6) assume the forms:

$$\text{Re}_x^{\frac{1}{2}} C_f = \left(\frac{\mu_{hnf}}{\mu_f} \right) f''(0), \text{Re}_x^{\frac{1}{2}} Nu_x = - \left(\frac{k_{hnf}}{k_f} \right) \theta'(0) \quad (12)$$

Where the local Reynolds number is $\text{Re}_x = \frac{2Lu_w}{v_f}$. The hybrid nanofluid variables arising in Eqns.

(7)-(12) are documented in **Table 1**, following Devi and Devi [47]. All parameters are defined in the nomenclature.

Table 1: Hybrid nanofluid Physical properties – see Devi and Devi [47]

Properties	Hybrid nanofluid
Density (ρ)	$\rho_{hnf} = \rho_{s1}\phi_{s1} + \rho_{s2}\phi_{s2} + \rho_f(1 - \phi_{hnf})$ where $\phi_{hnf} = \phi_{s1} + \phi_{s2}$
Viscosity (μ)	$\frac{\mu_{hnf}}{\mu_f} = \frac{1}{(1 - \phi_{hnf})^{2.5}}$
Heat Capacity (ρC_p)	$(\rho C_p)_{hnf} = (\rho C_p)_{s1}\phi_{s1} + (\rho C_p)_{s2}\phi_{s2} + (\rho C_p)_f(1 - \phi_{hnf})$
Thermal conductivity (K)	$\frac{k_{hnf}}{k_f} = \frac{\left[2k_f + \left(\frac{\phi_{s1}k_{s1} + \phi_{s2}k_{s2}}{\phi_{hnf}} \right) + 2(\phi_{s1}k_{s1} + \phi_{s2}k_{s2}) - 2\phi_{hnf}k_f \right]}{\left[2k_f - \left(\frac{\phi_{s1}k_{s1} + \phi_{s2}k_{s2}}{\phi_{hnf}} \right) - (\phi_{s1}k_{s1} + \phi_{s2}k_{s2}) + \phi_{hnf}k_f \right]}$

3. BOUNDARY VALUE PROBLEM AND NUMERICAL METHOD

The non-linear ordinary differential equations (7) and (8) subject to boundary conditions (12) have been solved computationally with the MATLAB-based bvp4c solver. The boundary value problem is reduced from a multi-degree ordinary differential equation system to a multiple first order system which is much more amenable to numerical solution. As such the present system of ordinary differential equations (7, 8) is converted into five first-order equations in stages 1 and 2. In stage 3, the boundary condition is transformed, and in stage 4, the bvp4c program is executed with all relevant parameter data to generate robust solutions. Actual thermophysical data for the considered hybrid nanofluid is given in **Table 2**.

Table 2: Nanoparticles and base fluid thermophysical properties

Properties	Al ₂ O ₃	Cu	H ₂ O
ρ	3970	8933	997.1
C_p	765	385	4179.0
K	40	400	0.6130
P_r	-	-	6.20

Stage 1: We have introduced the following components for the coupled nonlinear ordinary differential equations in equations (7), (8):

$$\left. \begin{array}{l} f = y(1), \\ f' = y(2), \\ f'' = y(3), \\ \theta = y(4), \\ \text{and } \theta' = y(5) \end{array} \right\} \quad (13)$$

Stage 2:

Now, inside the system of equations for the first order, we write these new variables as follows:

$$f' = y(2);$$

$$f'' = y(3);$$

$$f''' = \left(\frac{\rho_{mf} / \rho_f}{\mu_{mf} / \mu_f} \right) 2y(2)^2 - y(1)y(3) - Da y(2);$$

$$\theta = y(4);$$

$$\theta' = y(5);$$

$$\theta'' = \left(\frac{1}{\left(\frac{1}{\text{Pr}} \frac{k_{mf}}{k_f} - 0.25\alpha(y(1))^2 \right)} \right) \left(- \frac{(\rho C_p)_{mf}}{(\rho C_p)_f} \left(\frac{y(1)y(5) - y(2)y(4)}{y(2)y(4)} \right) - \beta y(4) + \alpha \begin{Bmatrix} 0.75y(1)y(2)y(5) + \\ 0.5(y(2))^2 \eta y(5) + \\ 0.5y(1)y(3)y(4) + \\ (y(2))^2 y(4) \end{Bmatrix} \right). \quad (14a-e)$$

Stage 3:

The boundary conditions are recast as the following, in line with the newly introduced variables in MATLAB bvp4c:

$$[ya(1) - S, ya(2) - \lambda - Aya(3), ya(4) - 1 - Bya(5), yb(20), yb(4)] \quad (15)$$

Stage 4:

The system of first-order equations (14a-e) is solved with conditions (15) using Matlab's bvp4c solver.

4. VALIDATION OF MATLAB BVP4C CODE

The present generalized model is novel and contains many new terms. Therefore, to validate we use two methodologies.

4.1 Benchmarking with previous study

First, we compare the MATLAB solution with a special case from the previous study. **Table 3** presents the results of the comparison with the previous study of Waini *et al.* [68] who considered unitary Al_2O_3 -water nanofluid. Clearly, a high level of agreement has been attained, confirming the legitimacy of the current MATLAB code. We consider the effect of only alumina nanoparticle volume fraction (in the absence of Soret and Dufour effects in [68]) on the reduced local Nusselt number, and it is evident that a decrease is induced i. e. heat transfer to the stretching surface ($\lambda = 1$ implies stretching) is decreased. This verifies that the temperature within the boundary layer rises as the volume fraction of alumina nanoparticles increases.

Table 3. Comparison of the values of $Re_x^{-1/2} Nu_x$ for base fluid when $\varphi_1 = 0.1, Du = Sr = Sc = 0$ and $\lambda = 1$ for different values of φ_2

φ_2	Du	Sr	Waini <i>et. al.</i> [68]	Present MATLAB BVP4C code
0	0	0	0.5739	0.573879
0.02			0.5734	0.573396
0.04			0.5724	0.572384

4.2 Full validation with Adams-Moulton 2-step predictor corrector algorithm (AMPC)

Secondly, we utilize an alternative numerical method, namely the **AMPC**. This technique has been used in several multi-physical flow problems in recent years and further information is provided in Umavathi *et al.* [10] and Bég [69]. Rather than switching off new terms in the general extended model defined by Eqns. (7)-(10), the verification approach used here has a significant advantage over reduced previous models from the works. This is because the model created in the present work can be validated, which means all the effects are included. One popular approach used in this model is the implicit multistep method adopted by Adams Moulton. Another variant is the AMPC approach, which is known for its rapid convergence and stability when applied to a linear initial value issue. With the use of this algorithm, the current boundary value problem can be solved efficiently and effectively. The important benefit of this verification approach is that it provides the opportunity for the current model to be validated with all effects included, so that it can be compared with earlier reduced models from the literature. A good example of this is Adams Moulton's implicit multistep approach. A popular variant of Adams Moulton's two-step approach for linear initial value problems is its rapid convergence, stability, and predictability. The current boundary value problem can be solved with this algorithm when it is applied to it. first, we specify the f and θ as follows:

$$\left. \begin{aligned} \frac{df}{d\eta} &= v(\eta, f), f(\eta_0) = f_0 \\ \frac{d\theta}{d\eta} &= v(\eta, \theta), \theta(\eta_0) = \theta_0 \end{aligned} \right\} \quad (16)$$

Here f_0, θ_0 , are initial assumptions. A stepping distance AMPC relationship for the four variables of ζ in the η -direction, have the following form:

$$\left. \begin{aligned} f_{k+1} &= f_k + \frac{\zeta}{2} (3v(\eta_k, f_k) - v(\eta_{k-1}, f_{k-1})) \\ \theta_{k+1} &= \theta_k + \frac{\zeta}{2} (3v(\eta_k, \theta_k) - v(\eta_{k-1}, \theta_{k-1})) \end{aligned} \right\} \quad (17)$$

The formulas for the two-step corrector are given by:

$$\left. \begin{aligned} f_{k+1} &= f_k + \frac{\zeta}{2} (v(\eta_{k+1}, f_{k+1}) - v(\eta_k, f_k)) \\ \theta_{k+1} &= \theta_k + \frac{\zeta}{2} (v(\eta_{k+1}, \theta_{k+1}) - v(\eta_k, \theta_k)) \end{aligned} \right\} \quad (18)$$

For all simulations, a constant solid volume fraction (ϕ_{s1}) for $\text{Al}_2\text{O}_3 = 0.01$ i. e. 1% doping, as recommended by Devi and Devi [47] is used. Additionally, we use the default copper nanoparticle concentration as (ϕ_{s2}) also of 0.01 i. e. 1%. The *solid/dashed lines* correspond to MATLAB BVP4C *first/second* solutions. The data utilized is summarized in **Table 4** unless otherwise indicated in any of the Tables or graphs.

A	B	β	S	Pr	α	λ
0.6	0.2	0.02	2.4	6.2	0.03	-1

Table 4: Parameter values utilized in MATLAB and AMPC simulations.

In order to ensure the correctness of the solutions obtained through MATLAB's BVP4C solver, a detailed comparative analysis has been performed with the Adams Moulton Predictor-Corrector scheme (AMPC) for Nu_x solutions. The comparative results have been presented in **Table 5** and **Table 6** for the upper and lower branch Cf solutions, which clearly shows the differences and similarities between the two methods in terms of their accuracy and reliability. MATHEMATICA software environment has been deployed to execute the AMPC code which runs efficiently on a HP laptop and compiles in seconds. Solutions are truncated at 4 decimal places.

Table 5: Nu_x for variation in stretching/shrinking parameter (λ) with fixed thermal slip (B) parameter.

λ	$B = 0.2$			
	Upper (first) branch solution-	Upper (first) branch solution-	Lower (second) branch solution-	Lower (second) branch solution-

	MATLAB BVP4C	AMPC Method	MATLAB BVP4C	AMPC Method
1	3.9745	3.9744	3.9642	3.9643
0.9	3.9731	3.9733	3.9628	3.9627
0.8	3.9718	3.9720	3.9612	3.9613
0.5	3.9676	3.9674	3.9564	3.9566
0.3	3.9647	3.9649	3.9529	3.9530
0	3.9599	3.9601	3.9473	3.9474
-0.3	3.9547	3.9541	3.9411	3.9412
-0.5	3.9510	3.9512	3.9367	3.9368
-0.7	3.9469	3.9469	3.9323	3.9323
-0.8	3.9447	3.9446	3.9301	3.9302
-1	3.9399	3.9398	3.9258	3.9259

Table 6: C_f for variation in stretching/shrinking parameter (λ) with fixed copper nanoparticle volume fraction ($\phi_{s2} = 0.5\%$).

λ	$\phi_{s2} = 0.005$			
	Upper (first) branch solution- MATLAB BVP4C	Upper (first) branch solution- AMPC Method	Lower (second) branch solution- MATLAB BVP4C	Lower (second) branch solution- AMPC Method
1	1.8750	1.8752	3.1305	3.1306
0.9	1.6757	1.6761	2.9394	2.9391
0.8	1.4786	1.4789	2.7513	2.7515
0.5	0.9022	0.9024	2.2070	2.2072
0.3	0.5316	0.5318	1.8624	1.8626
-0.3	-0.4963	-0.4966	0.9207	0.9204
-0.5	-0.8023	-0.8024	0.6276	0.6271
-0.7	-1.0824	-1.0826	0.3289	0.3292
-0.8	-1.2102	-1.2104	0.1722	0.1724
-1	-1.4322	-1.4325	-0.1720	-0.1725
-1.1	-1.5197	-1.5192	-0.3685	-0.3687

Inspection of **Table 5 and 6** confirms that excellent correlation is achieved between the MATLAB BVP4C and AMPC code computations. Confidence in both the first and second solutions for the generalized model defined by Eqns. (7)-(10) is therefore justifiably very high.

5. MATLAB BVP4C RESULTS AND DISCUSSION

Having established the validity of the MATLAB bvp4c solver in section 4, detailed computations have been visualized graphically in **Figs 2-13** using the bvp4c function in MATLAB.

To complete the Cu-Al₂O₃/water hybrid nanofluid, solid volume fraction, (ϕ_{s2}) for copper nanoparticles, Cu, is included. As noted earlier, in every graph, the continuous lines represent the initial solution, while the dashed lines represent the alternative solution. In dual solutions, multiple values of missing initial guesses are assumed to give two different solutions under the same circumstances. Both solutions are called upper or first-branch solutions, while the lower or second-branch solutions are called lower or second-branch solutions [62-65].

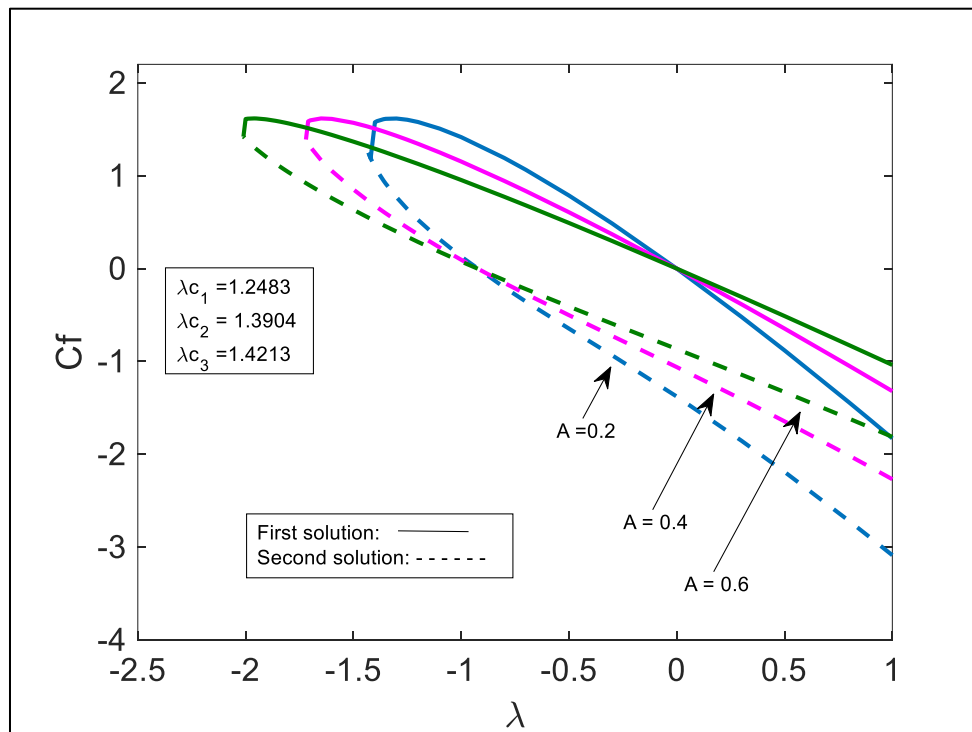


Fig 2: Skin-friction variation with stretching/shrinking parameter (λ) and hydrodynamic slip (A).

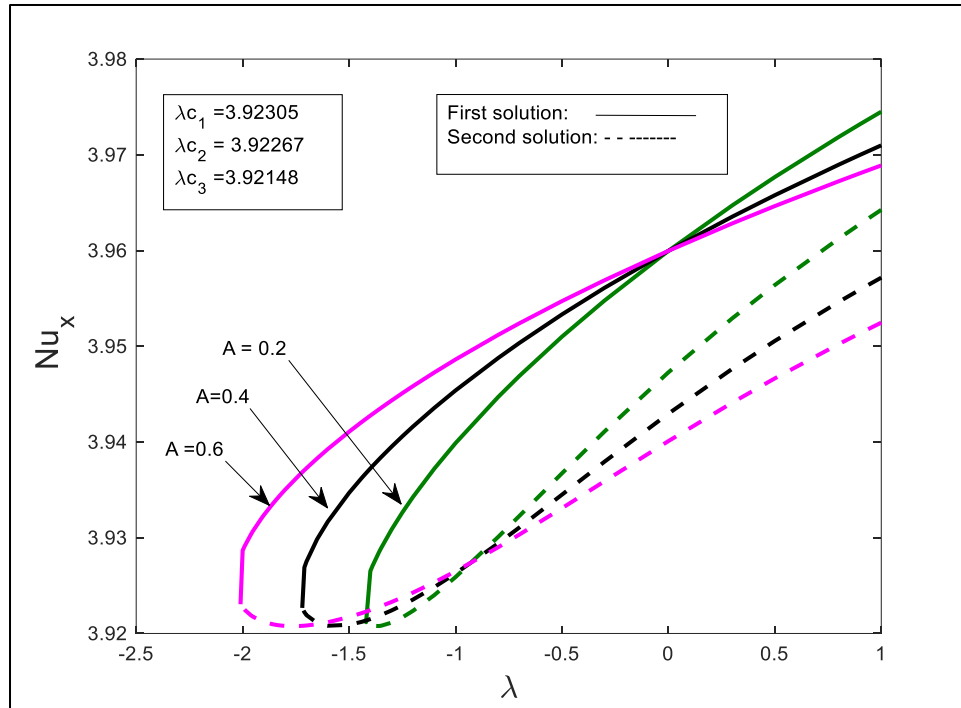


Fig 3: Nusselt number distribution with stretching/shrinking parameter (λ) and hydrodynamic slip (A).

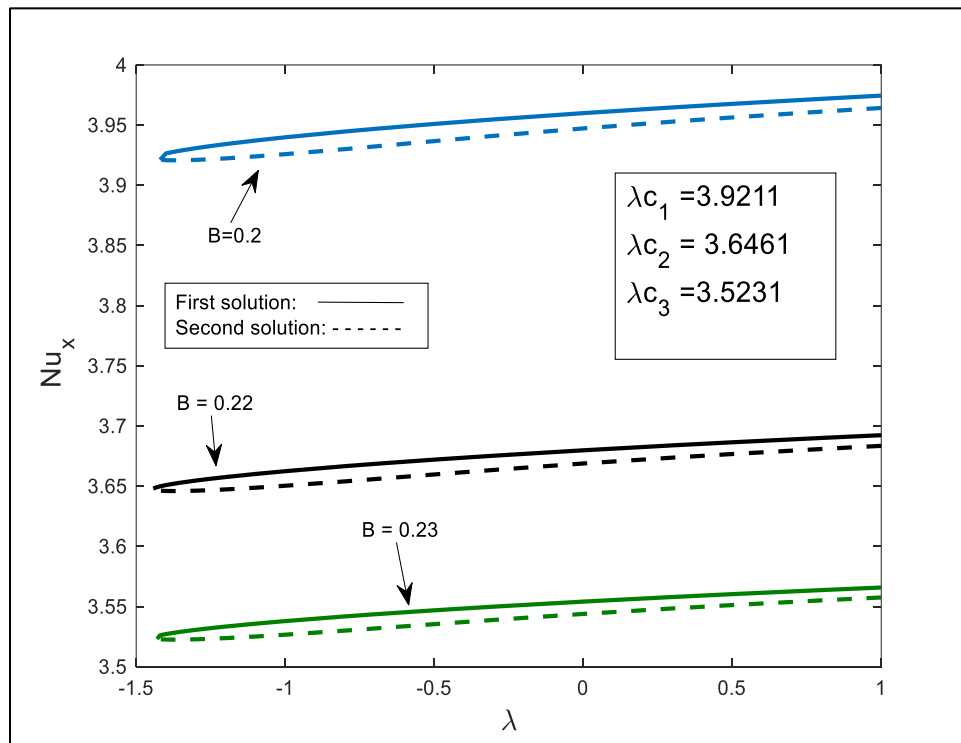


Fig 4: Nusselt number distribution with stretching/shrinking parameter (λ) and thermal slip (B).

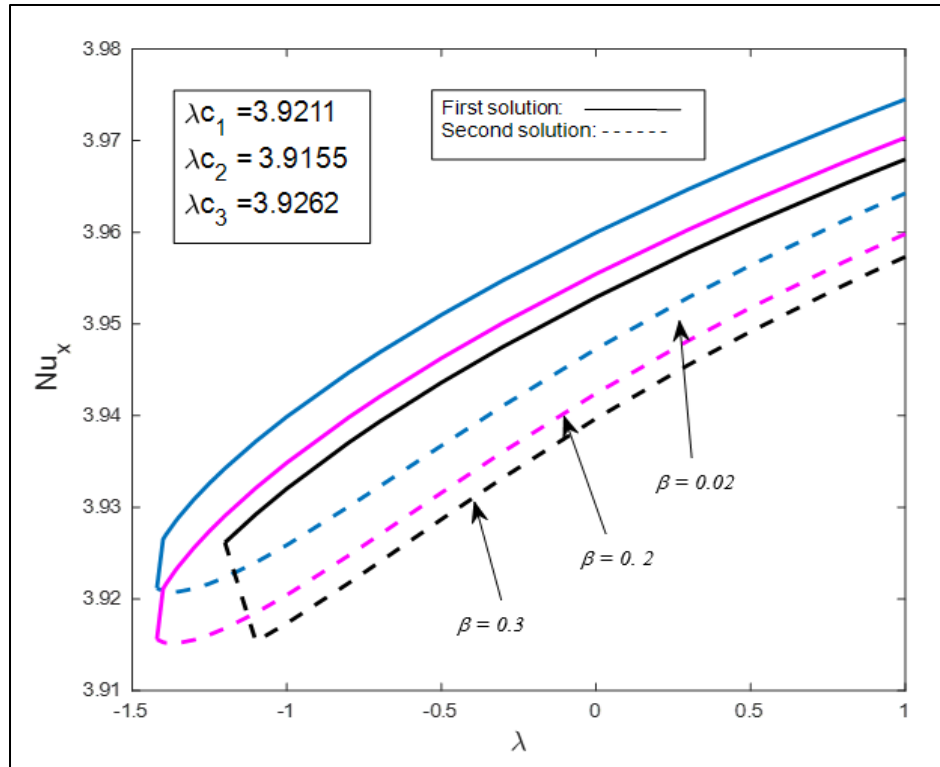


Fig 5: Nusselt number distribution with stretching/shrinking parameter (λ) and heat source (β).

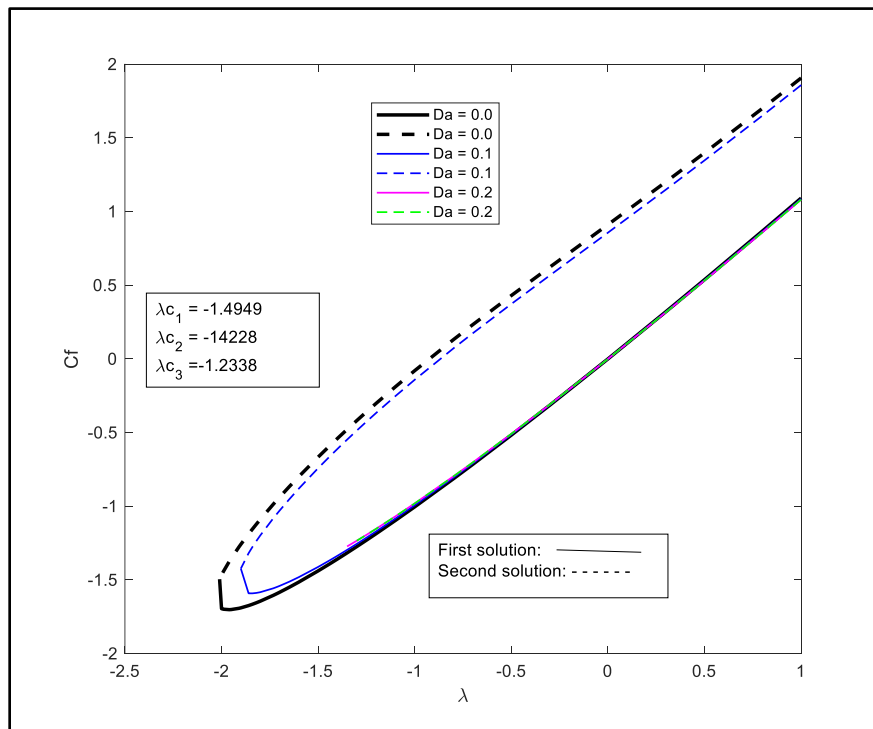


Fig 6: Skin-friction variation with stretching/shrinking parameter (λ) and Darcy number (Da).

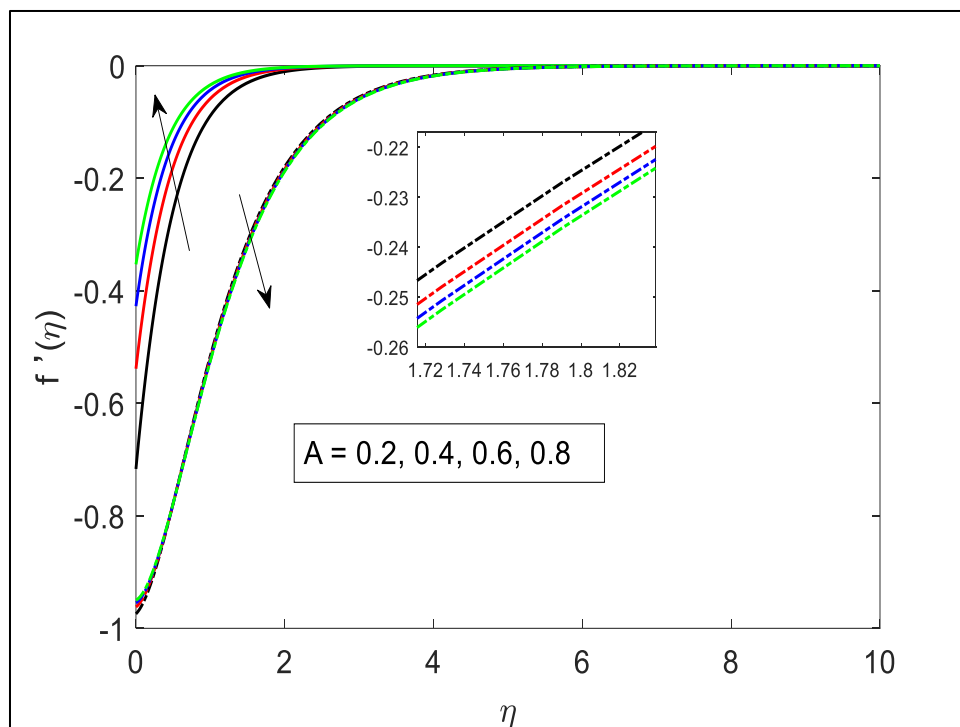


Fig 7: Velocity distribution with hydrodynamic slip (A).

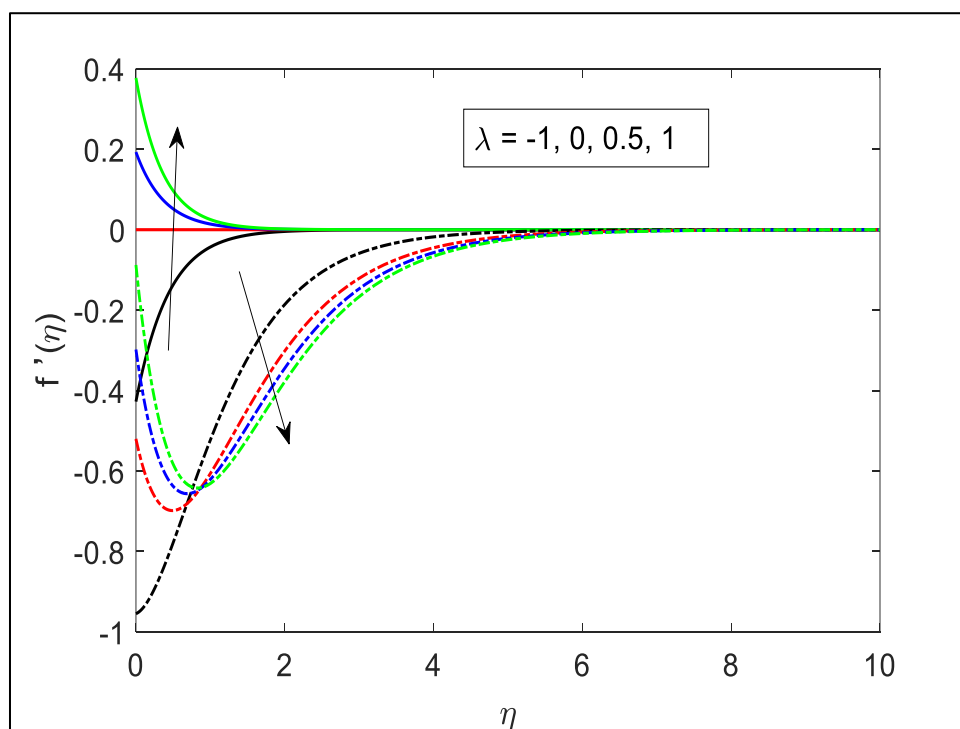


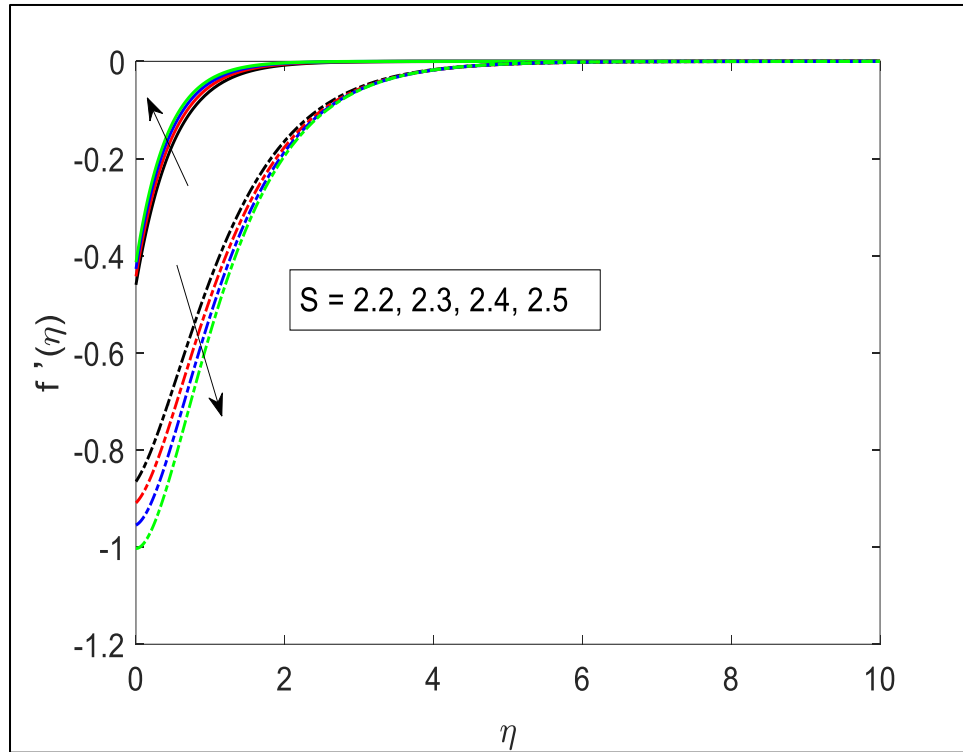
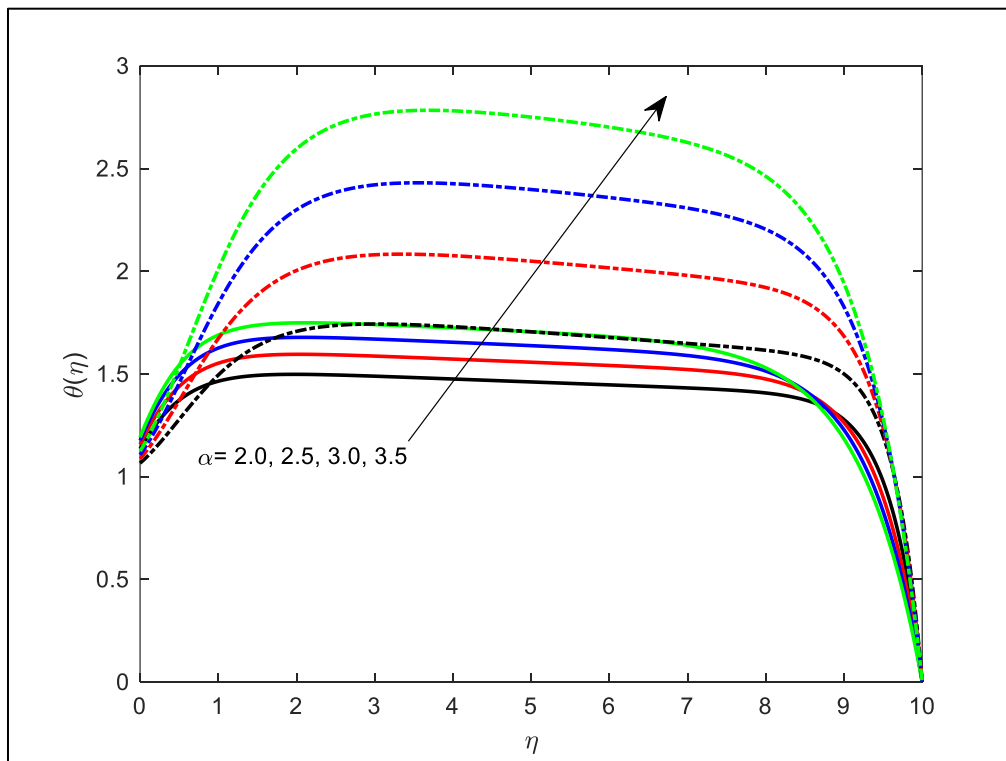
Fig 8: Velocity distribution with stretching/shrinking parameter (λ)**Fig 9:** Velocity distribution with wall suction parameter (S)

Fig 10: Temperature distributions with non-Fourier thermal relaxation parameter (α).

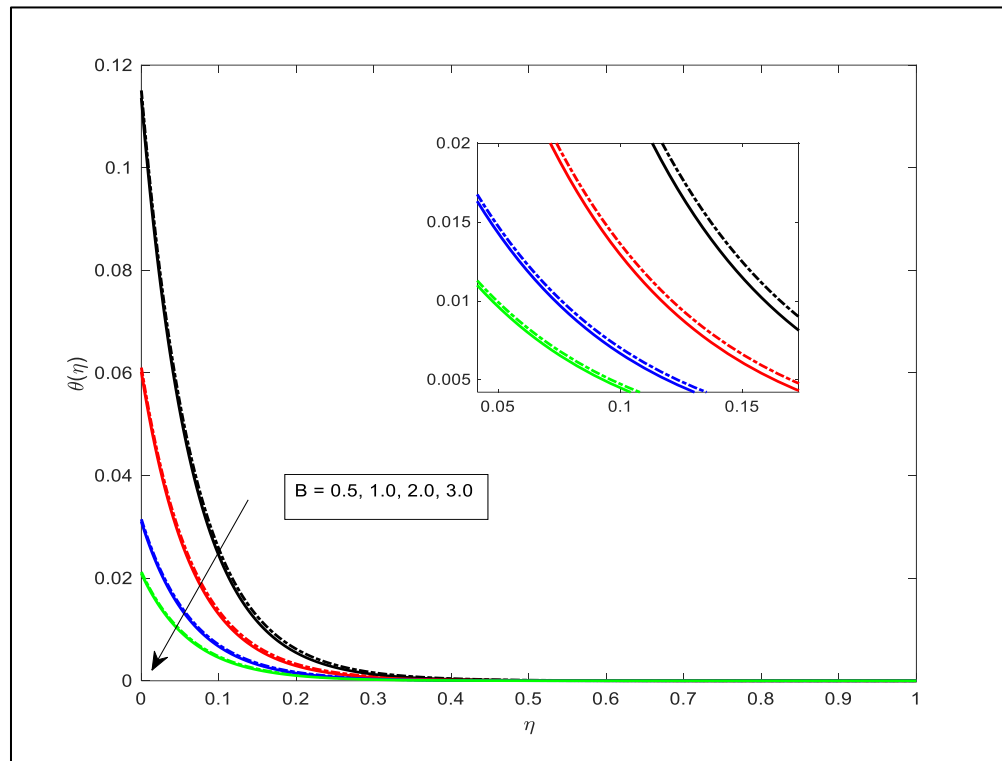


Fig 11: Temperature distributions with thermal slip parameter (B)

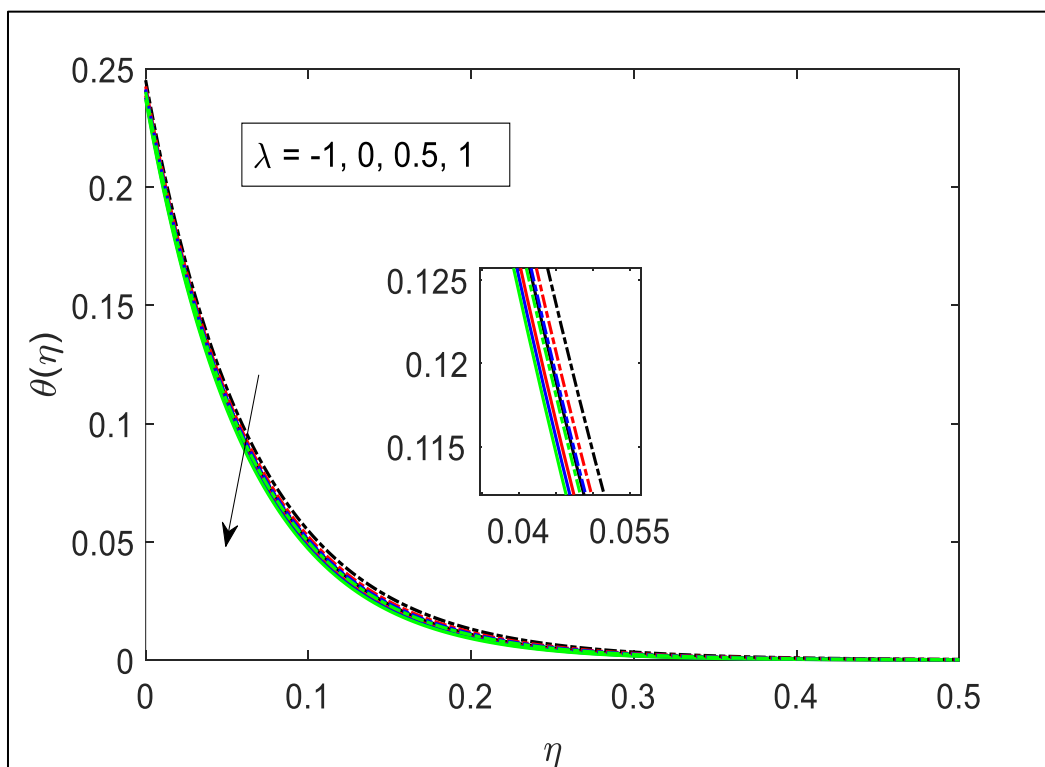
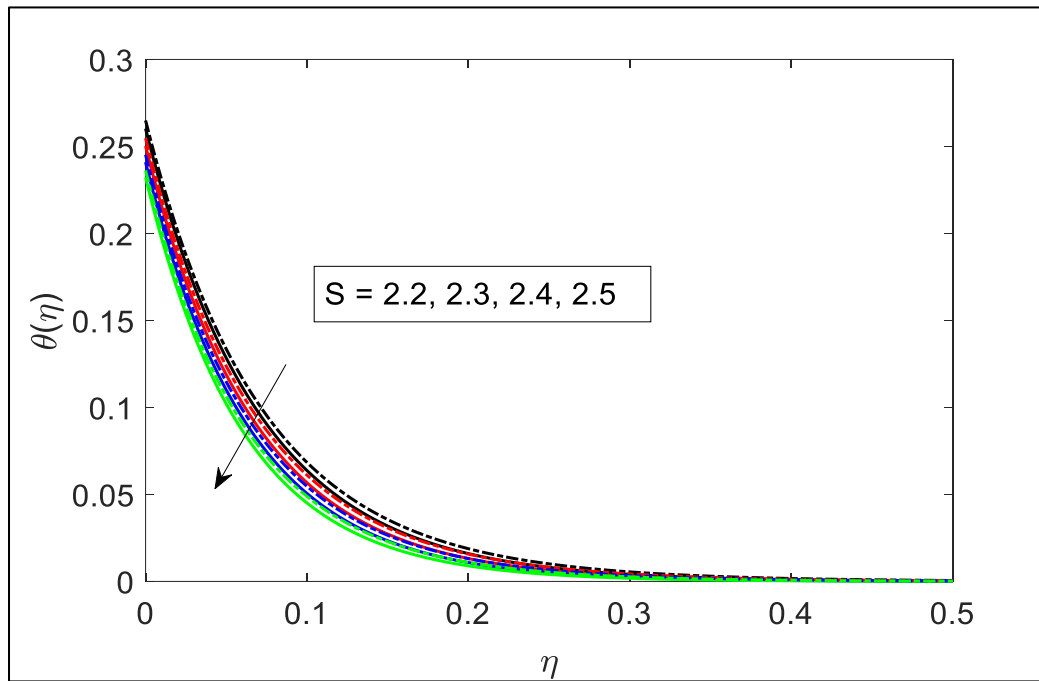


Fig 12: Temperature evolution with stretching/shrinking parameter (λ)**Fig 13:** Temperature profiles with wall suction parameter (S)

The outcomes for *skin friction coefficient*, C_f , and *reduced local Nusselt number*, Nu_x are plotted in **Figs. 2–5**, and solutions for velocity and thermal gradient are displayed in **Figs. 6–12**, for the impact of selected key control parameters.

Fig. 2 shows the response in skin-friction to unlike values of hydrodynamic slip parameter, A (0.2, 0.4, and 0.6) and also the stretching/shrinking parameter (λ). Both these parameters feature exclusively in the wall boundary conditions in eqn. (9), viz, $f(0) = S, f'(0) = \lambda + Af''(0)$. They do not appear in the actual momentum eqn. (7). For both the first (upper) and second (lower) branch solutions, skin friction is maximum for the shrinking sheet case ($\lambda < 0$) and minimal for the stretching sheet case ($\lambda > 0$). Clearly skin friction is elevated when the sheet contracts, but it is depleted when the sheet is extended. However, with increasing hydrodynamic slip (A), While the skin friction reduction is evident in both the initial and secondary solutions for the shrinking sheet scenario, in the case of the stretching sheet, both solutions exhibit an augmentation in skin friction with increased hydrodynamic slip (A). The branch solution is computed at the critical value of $\lambda = \lambda_c$. Clearly for $\lambda > \lambda_c$, several solutions exist. Thus, λ_c is connected to a delineation in the behavior of the skin friction with hydrodynamic slip effects. Generally, only for stretching will

greater hydrodynamic slip accelerate the boundary layer flow since momentum development will be assisted with extension of the substrate surface. However, deceleration is induced with greater hydrodynamic slip for the contracting sheet case.

Fig. 3 shows the distribution of local Nusselt number against stretching/shrinking parameter, λ , again with different values of hydrodynamic (velocity) slip parameter, A . Again, both upper and lower i. e. first and second solutions for Nusselt number, are minimized for the shrinking sheet case ($\lambda < 0$) whereas they are maximized for the stretching sheet ($\lambda > 0$) case. Furthermore, for $\lambda < 0$, dual solutions are increased with growing hydrodynamic slip (A), although the elevation in first (upper) solution is much more significant. A distinct crossover in behaviour is observed at $\lambda = 0$ (static undeformed sheet) and thereafter as stretching becomes more intensive the local Nusselt number is depleted with increment in hydrodynamic slip (A). However, the reduction is much less dramatic than the elevation for the shrinking sheet case. A much stronger suppression however in the lower branch (second) solution for local Nusselt number is observed with greater hydrodynamic slip (A) for the stretching case. Maximum local Nusselt number is therefore consistently computed for dual solutions at the maximum stretching parameter value ($\lambda=1$) and minimal hydrodynamic slip ($A = 0.2$). This implies that the peak transfer of heat to the wall (sheet) arises only for strong stretching and weak slip. This effectively implies maximum cooling in the nanofluid coating boundary layer regime.

Fig. 4 demonstrates how the local Nusselt number i. e. heat transfer rate to the wall (substrate surface) is affected by the combined impact of the thermal slip parameter (B) and the stretching/shrinking parameter (λ). Evidently again for $\lambda > \lambda_c$, there are several solutions computed. Thermal slip ascends again in the sheet boundary conditions (9), specifically as $\theta(0) = 1 + B\theta'(0)$. The topologies of dual solutions are very different from the previous graph where hydrodynamic slip was considered. In this case, generally linear profiles with a gentle gradient are computed as λ is increased. With greater thermal slip, both first and second solutions are decreased in magnitude for both cases. However, the magnitude of the upper branch (first) solution is always in excess of the lower branch (second) solution. Effectively heat transfer to the wall is depleted with greater thermal slip since temperatures in the boundary layer will be enhanced. Great magnitudes of Nu_x are calculated for the stretching wall case ($\lambda > 0$) compared with the shrinking sheet case ($\lambda < 0$). Overall, with elevation in thermal slip B (0.2, 0.4, 0.6), heat transfer rate to the boundary falls for the weaker (second) solution and increases for the stable (first) solution.

Fig. 5 visualizes the influence of heat source parameter, β (0.02, 0.2, and 0.3), on local Nusselt number plotted against stretching/shrinking parameter (λ). Significantly higher values of the upper branch (first) solution are computed at all values of stretching/shrinking parameter, relative to the lower branch (second) solution. Both solutions increase in a linear fashion with (λ); however, with augmentation in heat generation parameter there is a substantial depletion in the magnitudes of both solutions for local Nusselt number, regardless of whether the sheet is contracting or expanding. The presence of a hot spot produces an internal thermal source in the boundary layer. This elevates temperatures in the nanofluid coating and therefore reduces thermal transferred to the wall surface. Critical values of the stretching parameter at which the upper and lower branch solutions bifurcate are also given in the figure.

Fig. 6 visualizes the influence of porous parameter, Da (0.0, 0.1, and 0.3), on skin-friction plotted against stretching/shrinking parameter (λ). Significantly higher values of the upper branch (second) solution are computed at all values of stretching/shrinking parameter, relative to the lower branch (first) solution. Both solutions increase in a linear fashion with (λ); however, with increment in heat generation parameter there is a substantial depletion in the magnitudes of both solutions for skin-friction, regardless of whether the sheet is contracting or expanding.

Figure 7 displays the velocity progression with transverse coordinate (η) for various values of the hydrodynamic (momentum) slip parameter, A . Much higher velocity magnitudes arise as anticipated for the upper branch (stable) solution relative to the lower branch (weak) solution. Sigmoidal configurations are evident, displaying asymptotically smooth convergence within the free stream. This underscores the importance of incorporating a suitably broad infinity boundary condition within MATLAB's `bvp4c` computational domain. A strong elevation in velocity (upper solution) accompanies an increment in hydrodynamic slip since the non-adherence at the wall (substrate) encourages momentum development and induces an acceleration in the boundary layer flow. The thickness of the momentum boundary layer is consequently diminished in the nanofluid coating with greater momentum slip. A weak but non-trivial decrease in the lower branch (second) velocity solution however is computed with greater momentum slip.

Fig. 8 illustrates the distribution in upper and lower branch velocity solutions with stretching/shrinking parameter (λ). With regard to the upper branch solution (first stable solution),

for the shrinking sheet case ($\lambda = -1$), negative values (strong deceleration) are computed indicating flow reversal i. e. back flow at small values of the transverse coordinate (η). However, first solution velocity values rapidly converge to zero. For the static wall ($\lambda = 0$) zero values are computed for the upper branch solution at all values of transverse coordinate. However for the stretching wall case, strong acceleration is observed with positive values computed up to $\eta \sim 2$. For the lower branch solution (second unstable solution), velocity values are always negative irrespective of whether the sheet is shrinking, static or stretching. However, near the wall ($0 < \eta < 0.4$) stretching produces less deceleration whereas shrinking induces stronger deceleration (more negative values). Further from the wall, this trend is however reversed, and less negative values correspond to shrinking (black dashed line) whereas more negative values arise for stretching (green dashed line). Effectively the profiles for the lower branch solution only converge to zero after a much greater value of transverse coordinate is attained, approximately, $\eta = 6$. The presence of sheet (wall) stretching or shrinking therefore exerts a very significant impact on both upper and lower branch velocity solutions. Overall, much greater magnitudes are computed as before in earlier graphs, for the upper branch solution (stable) relative to the lower branch solution (unstable).

Figure 9 depicts the influence of wall suction/injection parameter, S on first and second order velocity solutions. Only suction is considered i. e. $S > 0$. Much greater values correspond to the first solution compared with the second solution. In both cases nevertheless the velocities are negative i. e. flow reversal arises. With increment in suction parameter, which features in the wall boundary condition, eqn. (9) i. e. $f(0) = S$, for the upper branch solution, increasing suction increases velocity and counteracts deceleration. Velocity values become progressively less negative as S is increased and asymptotically converge to zero rapidly at $\eta = 2$ approximately. Conversely for the lower branch solution, velocity is decreased i. e. values become more negative as S is increased. Profiles for the lower branch solution also take much longer to converge to the infinity boundary condition value of zero.

Figure 10 depicts the impact of non-Fourier TRT parameter (α) on first and second solutions for temperature, $\theta(\eta)$. This parameter arises in the modified terms, $-\alpha \left\{ \begin{array}{l} 0.75ff'\theta' + 0.5f'^2\eta\theta' + \\ 0.5ff''\theta + f'^2\theta + 0.25f^2\theta'' \end{array} \right\}$ in the thermal boundary layer eqn. (8). Both first and second solution magnitudes are elevated strongly with increasing non-Fourier thermal relaxation parameter (α). Significantly greater

magnitudes are computed for the lower branch solution and the profiles are also much more influenced over the same increment of α which is increased from 2 to 3.5. The upper branch (solid line) solutions are much more clustered over this range of variation. Overall, with greater thermal relaxation times, the temperature magnitudes are boosted. This confirms that the non-Fourier model (hyperbolic model with finite thermal wave speed propagation) correctly predicts higher temperatures than the classical Fourier model (parabolic model with infinite thermal wave speed propagation) which underpredicts them. Thermal boundary layer thickness will also be enhanced with greater non-Fourier TRT parameter values (α).

Figure 11 depicts the response in upper and lower branch temperature $\theta(\eta)$ solutions to a variation in thermal slip parameter, B . In all cases monotonic declines are calculated from the wall ($\eta=0$) to the free stream and smooth convergence is attained in an asymptotic manner. The lower branch (dashed line) solution achieves marginally higher magnitudes than the upper branch (solid line) solution. As thermal slip parameter is amplified there is a sustained drop in temperature magnitudes. Cooling is therefore induced within the nanocoating boundary layer with stronger thermal slip at the wall. This is due to the delay in heat convected from the wall to the boundary layer associated with thermal jump. More heat will be effectively retained at the boundary, resulting in a net heat transfer away from the boundary layer towards the substrate surface, thereby inducing a significant cooling effect. Consequently, the thermal boundary layer thickness will be reduced for both upper branch and lower branch scenarios.

Figure 12 shows the impact of stretching/shrinking parameter (λ) on the first (upper branch) and second (lower branch) temperature, $\theta(\eta)$. There is a distinct depletion in both temperatures with increment in λ . Higher magnitudes are computed for the lower branch solution compared with the upper branch (solid line) solution. The shrinking sheet case ($\lambda < 0$) exhibits higher temperatures and larger thermal boundary layer thickness than the stretching sheet case ($\lambda > 0$) with the static sheet case ($\lambda = 0$) falling between the two.

Fig. 13 depicts the influence of the wall suction parameter, S on first (upper branch) and second (lower branch) temperature, $\theta(\eta)$. With greater wall suction, S both first and second temperature solutions are consistently reduced. The imposition of lateral wall solutal flux out of the boundary layer causes the nanocoating to adhere more strongly to the substrate surface. This opposes momentum development and simultaneously induces a cooling effect leading to a reduction in

thermal boundary layer thickness. Again, slightly higher magnitudes are computed for the upper branch (first) solution relative to the lower branch (second) solution. MATLAB bvp4c successfully demonstrates a commendable convergence of profiles within the free stream (at the nanocoating boundary layer's edge). The results confirm the appropriateness of incorporating a sufficiently expansive infinity boundary condition in the simulations.

6. CONCLUDING REMARKS

A mathematical model for boundary layer coating flow of $\text{Al}_2\text{O}_3\text{-Cu-H}_2\text{O}$ hybrid binary nanofluid from an exponentially stretching porous substrate (sheet) has been presented. Lateral mass flux (suction) at the wall and heat source (generation) effects have been included. The Cattaneo-Christov heat flux non-Fourier model has been utilized which accurately incorporates thermal relaxation effects. The Tiwari-Das approach has been employed to formulate the nanoscale volume fraction for metallic nanoparticles, specifically Alumina (Al_2O_3) and Copper (Cu), dispersed in an aqueous base fluid (H_2O). The formulation incorporates hydrodynamic wall and thermal slip effects. The solution to the resulting non-dimensional transformed nonlinear coupled ordinary differential boundary value problem has been obtained using the efficient MATLAB bvp4c routine. Special cases of the non-Fourier model have been validated against published results, and the general model has been further validated using the robust Adams-Moulton 2-step predictor-corrector algorithm (AMPC). Dual solutions of the generalized model have been computed. A detailed study of key control parameters on momentum and thermal characteristics is conducted and solutions are visualized graphically. The computations have demonstrated that:

- It is possible to obtain dual solutions with suitable suction at the stretching surface, but only the first (upper branch) solution is stable.
- Elevated temperatures and increased thermal boundary layer thicknesses are determined for both the upper and lower branch solutions as the thermal relaxation parameter (Cattaneo-Christov hyperbolic model parameter) is augmented. This augmentation results in larger temperatures compared to those predicted by the classical Fourier parabolic heat conduction model.
- An increase in stretching parameter enhances the skin friction coefficient and elevates the local Nusselt number.

- With an elevation in wall suction, both first and second temperature solutions are consistently reduced as are thermal boundary layer thicknesses.
- An increase in wall suction produces a substantial enhancement in the first solution for velocity whereas it reduces the second solution velocity.
- Increased wall suction reduces temperatures and diminishes thermal boundary layer thicknesses.
- An augmentation in thermal slip, leads to a cooling in the nanocoating boundary layer is cooled i. e. temperature plummets and thermal boundary layer thickness is decreased.
- With larger values of heat generation (source) parameter there is a substantial reduction computed in both upper and lower branch local Nusselt number, regardless of whether the sheet is shrinking or stretching.
- Strong deceleration is induced with greater hydrodynamic (velocity) slip for both the upper and lower branch solutions.
- With greater velocity slip both the first (upper) and second (lower) solutions for skin friction are depleted with greater velocity slip for the shrinking case, whereas they are generally enhanced for the very strong stretching case.
- Both first and second solutions for skin friction are elevated with shrinking whereas they are depressed with stretching.

The present computations have offered some new insights into multi-physical thermal fluid dynamic of nanofluid-based coating systems. Both shrinking and stretching sheet cases have been considered. Both numerical methods, namely MATLAB bvp4c and AMPC have shown exceptional accuracy and stability in the simulations. However, attention has been confined to Newtonian non-magnetic nanofluids. Future studies may address a range of non-Newtonian models e. g. Maxwell viscoelastic nanofluids [20] and also ferromagnetic nanofluids [8,13, 14]. Additionally, Carreau nanofluids, as considered by Muhammad *et al.* [70] and exponential wall stretching as previously investigated by Ullah *et al.* [71] may also be explored. Efforts in these directions will be communicated imminently.

ACKNOWLEDGMENTS

The authors are grateful to reviewers for their comments which have improved the clarity of the present study.

REFERENCES:

- 1] A. Can, F. Selimefendigil, H.F. Oztop, A review on soft computing and nanofluid applications for battery thermal management, *J. Energy Storage* 53 (2022), 105214, <https://doi.org/10.1016/j.est.2022.105214>.
- 2] A.K. Hamzat, M.I. Omisanya, A.Z. Sahin, O.R. Oyetunji, N.A. Olaitan, Application of nanofluid in solar energy harvesting devices: a comprehensive review, *Energy Convers. Manag.* 266 (2022), 115790, <https://doi.org/10.1016/j.enconman.2022.115790>.
- 3] S.M. Hussain, W. Jamshed, R. Safdar, F. Shahzad, N.A.A. Mohd Nasir, I. Ullah, Chemical reaction and thermal characteristics of Maxwell nanofluid flow-through solar collector as a potential solar energy cooling application: a modified Buongiorno's model, *Energy & Environment*, 2022, 0958305X221088113, <https://doi.org/10.1177/0958305X221088113>.
- 4] J. Prakash, E.P. Siva, D Tripathi, S. Kuharat and O. Anwar Bég, Peristaltic pumping of magnetic nanofluids with thermal radiation and temperature-dependent viscosity effects: *modelling a solar magneto-biomimetic nanopump*, *Renewable Energy*, 133, 1308-1326 (2019). doi.org/10.1016/j.renene.2018.08.096 0960-1481
- 5] K.M. Jadeja, R. Bumataria, N. Chavda, Nanofluid as a coolant in internal combustion engine—a review, *Int. J. Ambient Energy* (2022) 1–18. <https://doi.org/10.1080/01430750.2022.2127891>
- 6] D. Tripathi, Noreen Akbar, O. Anwar Bég, Transient peristaltic diffusion of nanofluids: A model for micropumps in medical engineering, *J. Hydrodynamics*, 30(6): 774-781 (2018).
- 7] L.P. Wu, Z.J. Xie, G. Le et al., Investigation of the tribological behavior of graphene oxide nanoplates as lubricant additives for ceramic/steel contact. *Tribol. Int.* 128, 113–120 (2018)
- 8] A. Sumithra, R. Sivaraj, V. R. Prasad, O. Anwar Bég, Ho-Hon Leung, F. Kamalov, S.Kuharat and B.R. Kumar, Computation of inclined magnetic field, thermophoresis and Brownian motion effects on mixed convective electroconductive nanofluid flow in a rectangular porous enclosure with adiabatic walls and hot slits, *International Journal of Modern Physics B* (2024) 2450398 (30 pages) DOI: 10.1142/S0217979224503983 (30 pages)
- 9] Kim DM, Baek SW, Yoon J. Ignition characteristics of kerosene droplets with the addition of aluminum nanoparticles at elevated temperature and pressure. *Combust Flame* 2016; 173: 106–113.
- 10] J.C. Umavathi and O. Anwar Bég, Computation of thermo-solutal convection with Soret-Dufour cross diffusion in a vertical duct containing carbon/metallic nanofluids, *Proc. IMechE Part C- J. Mechanical Engineering* (2022). DOI: 10.1177/09544062211072693 (17 pages).

- 11] Tanvir S, Qiao L. Effect of addition of energetic nanoparticles on droplet-burning rate of liquid fuels. *AIAA J. Propulsion Power*, 2015; 31: 408–415.
- 12] H. R. Chauhan *et al.*, Role of micro- and nano-CeO₂ reinforcements on characteristics and tribological performance of HVOF sprayed Cr₃C₂-NiCr coatings, *Surface and Coatings Technology*, 467 (2023) 129684.
- 13] S.O. Solawu, M. Shamshuddin, O. Anwar Bég, Influence of magnetization, variable viscosity and thermal conductivity on Von Karman swirling flow of H₂O-Fe₃O₄ and H₂O-Mn-ZNFe₂O₄ ferromagnetic nanofluids from a stretchable rotating disk: smart spin coating simulation, *Materials Science and Engineering B*, 279 (2022) 115659 (13 pages).
- 14] J. C. Umavathi, O. Anwar Bég, Umar F. Khan, Tasveer A. Bég, Ali Kadir, Computation of swirling hydromagnetic nanofluid flow containing gyrotactic microorganisms from a spinning disk to a porous medium with Hall current and anisotropic slip effects, *ZAMM* (2023); DOI: 10.1002/zamm.202100575 (33 pages).
- 15] F. Ghadami, A. Zakeri, A.S.R. Aghdam, R. Tahmasebi, Structural characteristics and high-temperature oxidation behavior of HVOF sprayed nano-CeO₂ reinforced NiCoCrAlY nanocomposite coatings, *Surface and Coatings Technology*, 373 (2019), 7-16.
- 16] S. Sun, H. Fu, X. Ping, X. Guo, J. Lin, Y. Lei, W. Wu, J. Zhou, Effect of CeO₂ addition on microstructure and mechanical properties of in-situ (Ti, Nb)C/Ni coating, *Surface and Coatings Technology*, 359 (2019) 300-313.
- 17] M. Li, S. Zhang, H. Li, Y. He, J.-H. Yoon, T.-Y. Cho, Effect of nano-CeO₂ on cobalt-based alloy laser coatings, *J. Mater. Process. Technol.*, 202 (2008) 107-111.
- 18] R. Posner *et al.*, Corrosive delamination and ion transport along stretch-formed thin conversion films on galvanized steel, *Surface and Coatings Technology*, 253 (2014) 227-233.
- 19] R. van Tijum *et al.*, In-situ birefringence microscopy of uniaxially stretched metal–polymer laminate, *Surface and Coatings Technology*, 201 (2007) 4633-4639.
- 20] Muhammad Nasir, M. Waqas, O. Anwar Bég, Sami Znaidia, W. A. Khan and Nurnadiah Zamri, Functional magnetic Maxwell viscoelastic nanofluids for tribological coatings- a model for stretching flow using the generalized theory of heat-mass fluxes, Darcy-Forchheimer formulation and dual convection, *Tribology International*, 187 (2023) 108610 (14 pages). doi.org/10.1016/j.triboint.2023.108610
- 21] S. Qu *et al.*, Dynamic stretching–electroplating metal-coated textile for a flexible and stretchable zinc–air battery, *Carbon Energy*, 4 (5) 867-877 (2022).
- 22] Almansoori MT, Li X, Zheng L. A brief review on E-skin and its multifunctional sensing applications. *Curr Smart Mater.* 2019; 4(1): 3-14.

- 23] B. Venkateswarlu, P.V. Satya Narayana, Cu-Al₂O₃/H₂O hybrid nanofluid flow past a porous stretching sheet due to temperature-dependent viscosity and viscous dissipation, *Heat Trans.* 50 (5) (2020) 21884.
- 24] O. Anwar Bég, S. Kuharat, M. Ferdows, M. Das, A. Kadir, M. Shamshuddin, Magnetic nano-polymer flow with magnetic induction and nanoparticle solid volume fraction effects: *solar magnetic nano-polymer fabrication simulation*, *Proc. IMechE-Part N: J Nanoengineering, Nanomaterials and Nano-systems* (2019). DOI: 10.1177/ 2397791419838714 (19 pages)
- 25] B.K. Siddiqui, S. Batool, Q. Mahmood Ul Hassan, M. Malik, Repercussions of homogeneous and heterogeneous reactions of 3d flow of cu-water and al₂o₃-water nanofluid and entropy generation estimation along stretching cylinder, *Ain Shams Eng. J.*, 10.1016/j.asej.2021.05.007 (in press).
- 26] M. Garvandha, V. K. Narla, D. Tripathi and O. Anwar Bég, Modelling the impact of melting and nonlinear radiation on reactive Buongiorno nanofluid boundary layer flow from an inclined stretching cylinder with cross diffusion and curvature effects, In “*Energy Systems and Nanotechnology*”, *Advances in Sustainability Science and Technology Book Series, Springer-Germany Eds. D. Tripathi and S. Shamra*, pp.279-306 (2021).
- 27] M.J. Uddin, O. Anwar Bég and A.I. Ismail, Radiative-convective nanofluid flow past a stretching/shrinking sheet with slip effects, *AIAA J. Thermophysics Heat Transfer*, 29, 3, 513-523 (2015).
- 28] Nur Amalina Latiff, Md. Jashim Uddin, O. Anwar Bég and Ahmad Izani Md. Ismail, Unsteady forced bioconvection slip flow of a micropolar nanofluid from a stretching/ shrinking sheet, *Proc. IMECHE- Part N: J. Nanoengineering and Nanosystems*, 230 (4) pp. 177–187 (2016).
- 28] T. Thumma, O. Anwar Bég and A. Kadir, Numerical study of heat source/sink effects on dissipative magnetic nanofluid flow from a non-linear inclined stretching/shrinking sheet, *J. Molecular Liquids*, 232, 159-173 (2017).
- 29] Fourier JBJ. *Theorie analytique De La Chaleur*. Paris: Chez Firmin Didot (1822).
- 30] Cattaneo C. Sulla conduzione del calore. *Atti del Seminario Maermatico e Fisico dell Universita di Modena e Reggio Emilia* 1948; 3:83–101.
- 31] Christov CI. On frame indifferent formulation of the Maxwell–Cattaneo model of finite-speed heat conduction. *Mech Res Comm.* 2009; 36: 481–6.
- 32] Straughan B. Thermal convection with the Cattaneo–Christov model. *Int J Heat Mass Transfer* 2010; 53: 95–8.
- 33] Ciarletta M, Straughan B. Uniqueness and structural stability for the Cattaneo– Christov equations. *Mech Res Comm.*, 2010; 37: 445–7.

- 34] Tibullo V, Zampoli V. A uniqueness result for the Cattaneo–Christov heat conduction model applied to incompressible fluids. *Mech Res Comm.* 2011; 38:77–99.
- 35] Straughan B. Thermal convection with the Cattaneo–Christov model. *Int J Heat Mass Transfer* 2010; 53: 95–8.
- 36] Haddad SAM. Thermal instability in Brinkman porous media with Cattaneo–Christov heat flux. *Int J Heat Mass Transfer* 2014; 68: 659–68.
- 37] Hayat T, Ijaz Khan M, Farooq M, Alsaedi A, Waqas M, Yasmeen T. Impact of Cattaneo–Christov heat flux model in flow of variable thermal conductivity fluid over a variable thickness surface. *Int J Heat Mass Transfer*, 2016; 99:702–10.
- 38] Hayat T, Ijaz Khan M, Farooq M, Yasmeen T, Alsaedi A. Stagnation point flow with Cattaneo–Christov heat flux and homogeneous–heterogeneous reactions. *J Mol. Liq.* 2016; 220: 49–55.
- 39] M. Nasir, M. Waqas, O. Anwar Bég and N. Zamri, Homotopy analysis of mixed convection flow of a magnetized viscoelastic nanofluid from a stretching surface in non-Darcy porous media with revised Fourier and Fickian approaches, *Waves in Random and Complex Media (2023)*. DOI: 10.1080/17455030.2023.2178824
- 40] Gul, H., Ramzan, M., Chung, J.D. *et al.* Multiple slips impact in the MHD hybrid nanofluid flow with Cattaneo–Christov heat flux and autocatalytic chemical reaction. *Sci Rep* 11, 14625 (2021).
- 41] Yan Zhang, Nazia Shahmir, Muhammad Ramzan, Hammad Alotaibi, Hassan M. Aljohani, Upshot of melting heat transfer in a Von Karman rotating flow of gold-silver/engine oil hybrid nanofluid with Cattaneo-Christov heat flux, *Case Studies in Thermal Engineering*, 2021, Volume 26,101149.
- 42] Hassan Waqas, Taseer Muhammad, Sobia Noreen, Umar Farooq, Metib Alghamdi, Cattaneo-Christov heat flux and entropy generation on hybrid nanofluid flow in a nozzle of rocket engine with melting heat transfer, *Case Studies in Thermal Engineering*, 28, 2021, 101504.
- 43] Shaik Jakeer, P. BalaAnki Reddy, A.M. Rashad, Hossam A. Nabwey, Impact of heated obstacle position on magneto-hybrid nanofluid flow in a lid-driven porous cavity with Cattaneo-Christov heat flux pattern, *Alexandria Engineering Journal*, 60, 2021, 821-835.
- 44] Khursheed Muhammad, T. Hayat, S. Momani, S. Asghar, FDM analysis for squeezed flow of hybrid nanofluid in presence of Cattaneo-Christov (C-C) heat flux and convective boundary condition, *Alexandria Engineering J.*, 61, Issue 6, 2022, Pages 4719-4727.
- 45] G. Kumaran, R Sivaraj, V. Ramachandra Prasad, O. Anwar Bég, Numerical study of axisymmetric magneto-gyrotactic bioconvection in non-Fourier tangent hyperbolic non-functional reactive coating flow of a cylindrical body in porous media, *European Physical Journal Plus*, 136, 1107 (2021). <https://doi.org/10.1140/epjp/s13360-021-02099-z> (32 pages)

- 46] J. Prakash, D. Tripathi, O. Anwar Bég, V. Srivastava, EMHD Casson hybrid nanofluid flow over an exponentially accelerated rotating porous surface, *J. Porous Media*, 25(4):1–24 (2022).
- 47] Devi, S.A.; Devi, S.S.U. Numerical investigation of hydromagnetic hybrid Cu-Al₂O₃ /water nanofluid flow over a permeable stretching sheet with suction. *Int. J. Nonlinear Sci. Numer. Simul.* 2016, 17, 249–257.
- 48] MD. Shamsuddin, Nevzat Akkurt, O. Anwar Bég, Henry J. Leonard and Tasveer A. Bég, Analysis of unsteady rotating thermo-solutal MoS₂-EO Brinkman electro-conductive nanofluid transport with heat source, radiative and chemical reaction effects: Modelling a hybrid rotating nanofluid Hall MHD generator, *Partial Differential Equations in Applied Mathematics*, 7 (2023) 100525 (13 pages) doi.org/10.1016/j.padiff.2023.100525
- 49] Jayati Tripathi, B. Vasu, O. Anwar Bég, R.S.R. Gorla and P.K. Kameswaran, Computational simulation of rheological blood flow containing hybrid nanoparticles in an inclined catheterized artery with stenotic, aneurysmal and slip effects, *Computers in Biology and Medicine*, 139, 105009 (2021). (20 pages). doi.org/10.1016/j.compbio.2021.105009
- 50] J. Prakash, Dharmendra Tripathi, O. Anwar Bég, A.K. Tiwari and R. Kumar, Thermo-electro kinetic rotating non-Newtonian hybrid nanofluid flow from an accelerating vertical surface, *Heat Transfer* (2021). DOI: 10.1002/htj.22373 (32 pages)
- 51] W. Al-Kouz, A. Abderrahmane, M. Shamsuddin, O. Younis, S. Mohammed, O. Anwar Bég, D. Toghraie, Heat transfer and entropy generation analysis of water-Fe₃O₄/CNT hybrid magnetic nanofluid flow in a trapezoidal wavy enclosure containing porous media with the Galerkin finite element method, *European Physical Journal Plus* (2021). 136:1184 <https://doi.org/10.1140/epjp/s13360-021-02192-3> (23 pages)
- 52] Rishu Gandhi, B. K. Sharma, Chandan Kumawat and O. Anwar Bég, Modelling and analysis of magnetic hybrid nanoparticle (Au-Al₂O₃/blood) based drug delivery through a bell-shaped occluded artery with Joule heating, viscous dissipation and variable viscosity effects, *Proc. IMechE-Part E-J. Process Mechanical Engineering* (2021). DOI: 10.1177/09544089221080273 (20 pages)
- 53] M. M. Bhatti, O. Anwar Bég and Sara I. Abdelsalam, A computational framework of magnetized MgO-Ni/Water based hybrid nanofluid stagnation flow on an elastic stretching surface through a porous medium with application in solar energy coatings, *Nanomaterials. Special issue- "The role of nanofluids in renewable energy engineering"* (2022). <https://doi.org/10.3390/xxxxx> (22 pages)
- 54] U.S. Mahabaleswar, O. Anwar Bég, D. Baleanu and T. Anusha, Impact of Navier's slip and chemical reaction on the hydromagnetic hybrid nanofluid flow and mass transfer due to porous stretching sheet, *Sci. Reports*, 12:10451 (2022). 14 pages doi.org/10.1038/s41598-022-14692-y
- 55] M. M. Bhatti, O. Anwar Bég, R. Ellahi, M.H. Doranehgard, Faranak Rabiei, Electro-magneto-hydrodynamics hybrid nanofluid flow with Gold and Magnesium oxide nanoparticles

through vertical parallel plates, *J. Magnetism Magnetic Materials*, 564 (2022) 170136. doi.org/10.1016/j.jmmm.2022.170136 (12 pages)

56] K. Thirumalaisamy, R. Sivaraj, V. R. Prasad, O. Anwar Bég, Ho-Hon Leung, Firuz Kamalov and R. Panneer Selvam, Comparative heat transfer analysis of electroconductive water and kerosene hybrid nanofluids in a square porous cavity using the non-Fourier heat flux model, *Phys. Fluids*, 34, 122016 (2022) (24 pages). doi.org/10.1063/5.0127463

57] A.Sumithra, R. Sivaraj, V. Ramachandra Prasad, O. Anwar Bég, Ho-Hon Leung, F. Kamalov and S. Kuharat, Computational study of MHD mixed convective flow of Cu/Al₂O₃-water nanofluid in a porous rectangular cavity with slits, viscous heating, Joule dissipation and heat source/sink effects, *Waves Random Complex Media* (2023). DOI: 10.1080/17455030.2023.2168786 (34 pages)

58] K. Venkatadri, Hakan F. Öztop, V. Ramachandra Prasad, S. Parthiban and O. Anwar Bég, RSM-based sensitivity analysis of hybrid nanofluid MHD flow in an enclosure filled with non-Darcy porous medium using the Lattice Boltzmann Method, *Numerical Heat Transfer – A* (2023). doi.org/10.1080/10407782.2023.2193708

59] K. Bhagya Swetha Latha, M. Gnaneswara Reddy, D. Tripathi, O. Anwar Bég, S. Kuharat, Computation of stagnation coating flow of electro-conductive ternary Williamson hybrid GO-Au-CO₃O₄/EO nanofluid with a Cattaneo-Christov heat flux model and magnetic induction, *Nature-Scientific Reports* (2023). 13, Article number: 10972 (2023) (26 pages).

60] M.G. Reddy, D. Tripathi and O. Anwar Bég, Numerical modelling of electromagnetohydrodynamic (EMHD) radiative transport of hybrid Ti₆Al₄V-AA7075/H₂O nanofluids from a Riga plate sensor surface, *Chapter 12 in D. Tripathi et al. (eds.), Nanomaterials and Nanoliquids: Applications in Energy and Environment, Advances in Sustainability Science and Technology*, https://doi.org/10.1007/978-981-99-6924-1_12 (2024). (24 pages)

61] F. A. A. Elsebaee, *et al.*, Motile microorganism-based trihybrid nanofluid flow with an application of magnetic effect across a slender stretching sheet: numerical approach, *AIP Adv.*, vol. 13, no. 3, 2023. DOI: 10. Q7 1063/5.0144191.

62] Mousavi, S. M. *et al.* Dual solutions for Casson hybrid nanofluid flow due to a stretching/shrinking sheet: A new combination of theoretical and experimental models. *Chin. J. Phys.* 71, 574–88 (2021).

63] M. Rifat, H. Rubel, M. Ferdows, T. Tazin, T.A. Bég, O. Anwar Bég and Ali Kadir, Computation of stagnation point convection flow of CNT-nanofluids from a stretching sheet with melting: dual solutions, *ASME Open J. Engineering*, 2, 021052.1-14 (2023) (14 pages).

64] De, P., Mondal, H. & Bera, U. K. Dual solutions of heat and mass transfer of nanofluid over a stretching/shrinking sheet with thermal radiation. *Meccanica* 51, 117–24 (2016)

- 65] M. Ferdows, Tahia Tazin, K. Zaimi, O. Anwar Bég and T.A. Bég, Dual solutions in Hiemenz flow of an electro-conductive viscous nanofluid containing elliptic single-/multi-wall carbon nanotubes with magnetic induction effects, *ASME Open J. Engineering*, 1, 011040.1-14 (2022).
- 66] Amit Kumar Pandey, Sohita Rajput, Krishnendu Bhattacharyya, Ali J. Chamkha, Dhananjay Yadav, Potential impacts of Cattaneo–Christov model of heat flux on the flow of Carreau–Yasuda fluid with mixed convection over a vertical stationary flat plate, *Forces in Mechanics*, 11,2023,100179.
- 67] Hayat, T., Qasim, M., & Mesloub, S., MHD flow and heat transfer over permeable stretching sheet with slip conditions. *Int. J. Numerical Methods in Fluids*, 2011, 66(8), 963-975.
- 68] Waini, I., Ishak, A., & Pop, I. (2021). Dufour and Soret effects on Al₂O₃-water nanofluid flow over a moving thin needle: Tiwari and Das model. *International Journal of Numerical Methods for Heat & Fluid Flow*, 31(3), 766–782.
- 69] O. Anwar Bég, Numerical methods for multi-physical magnetohydrodynamics, *J. Magnetohydrodynamics and Plasma Research*, 18 (2) (2013) 93-200.
- 70] Abidin, M. Z., Ullah, N., Hussain, A., Saadaoui, S., Mohamed, M. M. I., & Deifalla, A. (2023). Case study of entropy optimization with the flow of non-Newtonian nanofluid past converging conduit with slip mechanism: An application of geothermal engineering. *Case Studies in Thermal Engineering*, 52, 103764. <https://doi.org/10.1016/j.csite.2023.103764>
- 71] Ullah, N., Marwat, D. N. K., Mohamed, M. M. I., & Moussa, S. B. (2024). Steady flow of thin film over porous moving and non-flat sheet with nonlinear kinematics of exponential type. *ZAMM-Journal of Applied Mathematics and Mechanics/Zeitschrift für Angewandte Mathematik und Mechanik*, 104(1), e202300057. <https://doi.org/10.1002/zamm.202300057>